PSFC/JA-05-38

Divertor physics research on Alcator C-Mod

B. Lipschultz, B. LaBombard, J.L. Terry, C. Boswell, I.H. Hutchinson

Plasma Science and Fusion Center
Massachusetts Institute of Technology
Cambridge MA 02139 USA

This work was supported by the U.S. Department of Energy, Grant No. DE-FC02-99ER54512. Reproduction, translation, publication, use and disposal, in whole or in part, by or for the United States government is permitted.

Divertor physics research on Alcator C-Mod

B. Lipschultz, B. LaBombard, J.L. Terry, C. Boswell, I.H. Hutchinson

Massachusetts Institute of Technology Plasma Science & Fusion Center, Cambridge Ma. 02139, USA

Corresponding author –
Bruce Lipschultz
NW17-103,
Massachusetts Institute of Technology
Plasma Science & Fusion Center,
Cambridge Ma. 02139
617-253-8638 (Phone)
617-253-0627 (FAX)
blip@psfc.mit.edu

Pages – 45 (for body, 29 more for figures)
Tables – 0
Figures – 29 (no color figures in printed manuscript)

Divertor physics research on Alcator C-Mod

B. Lipschultz, B. LaBombard, J.L. Terry, C. Boswell, I.H. Hutchinson

Massachusetts Institute of Technology Plasma Science & Fusion Center, Cambridge Ma. 02139, USA

Many important contributions to the understanding of divertor physics are presented in this review of Alcator C-Mod research. The three regimes of parallel transport, sheath-limited, conduction-limited and detached, were identified experimentally along with their effects on plasma pressure along the magnetic field in the Scrape-Off-Layer (SOL). The extensive probe and bolometric coverage of the divertor allowed detailed characterization of the physics of detachment. The ability to dissipate ITER-like parallel power densities with extremely high divertor radiation emissivities (> 40 MW/m^3) was demonstrated under high-recycling and detached divertor conditions. The vertical plate divertor concept, developed and applied first on C-Mod, allowed the effect of divertor geometry to be studied, with the result that the vertical-plate and deep-slot geometries have a lower detachment threshold than the standard, flat-plate divertor. High density ($n_e > 1x10^{21}$ m^{-3}) divertor conditions allowed recombination to be more clearly observed in C-Mod than elsewhere. That, together with the development of spectroscopic techniques, enabled the only quantitative measurements of ion loss rate via recombination (and its role in detachment) as well as the trapping of hydrogenic Lyman alpha radiation. These were both shown to have important roles in detachment physics.

I. Introduction

There is a large amount of experience studying edge physics issues at MIT. Research using the predecessor tokamak, Alcator C, concentrated on the study of poloidal asymmetries [1], the physics of MARFEs [2,3], as well as impurity generation [4] and transport [5,6]. This work was expanded to divertor studies with the conceptual development of the vertical-plate divertor for Alcator DCT [7-9] and CIT,[10,11] which eventually led to the building of Alcator C-Mod.

The C-Mod divertor plate configuration, the first so-called 'vertical-plate divertor' (Figure 1) is now adopted, or is in the process of being adopted by most divertor tokamaks due to its recognized advantages. The C-Mod design is particularly flexible, in that it allows comparisons of different divertor plate geometries in the same device. This has allowed the C-Mod researchers to answer questions about the effects of geometry on edge transport (plasma, neutrals, impurities) and divertor detachment. Alcator C-Mod, with its high plasma density, high parallel heat flux, low divertor plasma temperature and high-Z molybdenum first wall, is a unique facility among the world's divertor machines. Such features have demonstrated the high-Z divertor option (with boronized surfaces), where negligible erosion levels at material surfaces can be achieved while maintaining hot central temperatures with low levels of radiation from metals.

The study of divertor physics was a central focus of the C-Mod program from its inception in 1993. This is due to the general focus in the tokamak community and the unique aspects of C-Mod (divertor geometry, densities, wall material).

II. General divertor characteristics

The C-Mod divertor and SOL diagnostic complement were rapidly brought online enabling the C-Mod divertor research team to quickly identify important aspects of divertor physics. This is particularly true for probe measurements. Plasma conditions at divertor plate surfaces, measured by Langmuir probes (see Fig. 2a), were compared directly to those measured 'upstream' on the same flux surfaces by a scanning Langmuir probe. Figure 3 displays electron pressure and temperature profiles from the two sets of probe diagnostics (divertor and SOL) for three values of central line-averaged density. The electron pressure at the divertor plate is multiplied by a factor of 2 to account for the sound-speed flow there. The data is plotted as a function of ρ, the distance of a given flux surface from the separatrix referenced to their midplane values.

Three regimes of parallel plasma transport to the divertor surface can clearly be identified in Figure 3 for 800 kA plasmas. These regimes depend not only on the central density in these discharges but also on the flux surface location:

Sheath-limited regime: Profiles at low density, $\bar{n}_e \leq 10^{20}$ m^{-3} ($n/n_{Greenwald} \leq 0.17$),, exhibit an electron temperature that is nearly constant along the magnetic field lines for $\rho > 5$ mm due to an electron-ion collisional mean free path that is long compared to the connection length. Electron pressure is also constant along the magnetic field, **B**. The divertor sheath appears to support all of the temperature drop on these flux tubes thus limiting the power flow to the plate. Electron temperatures everywhere are the hottest in this low-density or 'sheath-limited' power flow regime.

High recycling regime: Profiles at moderate density, $1.0 \leq \bar{n}_e \leq 1.8 \times 10^{20}$ m^{-3} ($0.17 \leq n/n_{Greenwald} \leq 0.31$), with increased collisionality, show a 'high recycling' divertor condition across the profile: the electron temperature falls at the divertor plate relative to 'upstream'

while the density there has the opposite trend so as to keep pressure approximately constant along the magnetic field, B. A temperature gradient arises along the field line because parallel electron thermal conduction is poorer at lower temperatures ($\kappa_{//} \propto T^{5/2}$), while the divertor sheath temperature can remain low since it conducts heat more readily at the higher densities. The high recycling condition is seen in portions of the other profiles also: near the separatrix in the low density case and at large values of ρ in the highest density case.

Detached plasma regime: Profiles at high density, $\bar{n}_e \geq 1.8 \times 10^{20}$ m^{-3} ($n/n_{Greenwald} \geq 0.31$), show a 'detached divertor' condition over some portion of the profile. Both the divertor electron temperature and the plasma density are very low in this regime, clearly violating constant pressure along **B**. *The details of detachment physics are described in much more detail in sections V-X.*

III. Effect of field reversal

A number of asymmetries between inner and outer divertors are commonly observed in tokamaks. They include such characteristics as density, temperature, heat flux, radiation, degree of detachment [12], and C/H co-deposition [13]. The physics underlying the asymmetries is still under investigation utilizing both modeling and experiment. Such asymmetries were characterized early in C-Mod's operation and presented in several papers by Hutchinson [14,15] and LaBombard [16]. These papers were the first detailed experimental examination of the role of thermo-electric currents and drifts and so spawned modifications of 2-D edge codes to include such effects and study them as well. A novel hypothesis examined in [16] was the idea of asymmetric parallel transport to the divertor legs, which had not received much attention. For example, currents

flowing along field lines may contribute to asymmetric parallel heat fluxes. In the case of particle flows, imbalanced ionization sources can drive asymmetric parallel particle fluxes.

Detailed measurements of the inside/outside divertor asymmetry in Alcator C-Mod have been made with Langmuir probe systems, TV cameras, and tomographic bolometer and H_α systems [15]. Here we concentrate on the divertor Langmuir probe measurements.

Figure 4 shows cross-field profiles of electron stagnation pressure, electron temperature, and density at 3 poloidal locations: scanning probe ('upstream' just outside the divertor), outer divertor surface and inner divertor surface. Data are shown from two Ohmic, L-mode discharges (5.3 Tesla, 0.8 MA, $\bar{n}_e$ =0.9x10^{20} m^{-3}). With B_T in the normal direction (BxVB ion drift towards the lower x-point), the outer divertor plasma is significantly hotter than the inner divertor plasma (factor of 5-10). On the other hand, the plasma density is lower at the outer divertor such that the electron stagnation pressure is approximately the same and matches the pressure at the scanning probe location. With reversed B_T, the inner divertor generally becomes hotter than the outer divertor. The density asymmetry also reverses so that again the electron stagnation pressure approximately matches.

Figure 5 shows the dependence of the divertor asymmetry on edge plasma conditions, as recorded by the outside/inside temperature and density ratios (Fig. 5a,b) on the ρ = 4.5 mm flux surface. Ohmic, L-mode discharges are shown (5.3 Tesla, 0.8 MA, $0.6 \leq \bar{n}_e \leq 2.1$x10^{20} m^{-3}). The horizontal axis is the electron-ion mean free path at the scanning probe location (ρ = 4.5 mm), normalized to 1/2 the total parallel connection length between divertor plates (λ_{ei}/L). Low density discharges with a hot SOL (high λ_{ei}/L) display a large asymmetry, having outside/inside T_e ratios approaching ~10 with normal B_T and ~0.2 with reversed B_T. As the collisionality in

the SOL increases, the magnitude of the asymmetry decreases, vanishing in the highest density (lowest edge temperature) discharges.

The data in Figures 5c-d are indicative that thermo-electric currents are significant. J_{gnd} is defined as the current density on a divertor probe when the probe is biased at the potential of the divertor. A positive number indicates a net ion collection locally on the divertor surface. Contributions to J_{gnd} include: parallel currents flowing as a result of the inside/outside electron temperature differences (thermoelectric effect), loop-voltage induced parallel currents, and non-ambipolar currents (such as Pfirsch-Schluter currents) that flow partly parallel to B but complete the electrical circuit via cross-field transport.

Figures 5c and 5d show that a significant component of J_{gnd} exhibits a thermoelectric-like effect, scaling with the magnitude of the outside/inside electron temperature asymmetry and reversing when the asymmetry reverses. When the temperature asymmetry is high, J_{gnd} on the hotter divertor surface is negative (net electron collection) with a magnitude that can exceed twice the local ion saturation current density. When the temperature asymmetry vanishes ($\lambda_{ei}/L \leq 0.02$), J_{gnd} becomes independent of the direction of B_T, revealing a residual non-ambipolar component of $J_{gnd}/J_{sat} \sim -0.8$ for the outer and ~ -0.3 for the inner divertor locations.

The interpretation of the above data is still somewhat open. At the lower densities, where the imbalance is large enough to detect the difference between power imbalance and pressure imbalance, the measurements indicate that pressure is not imbalanced but power is [14]. Thus power asymmetries seem a potential source of the observed asymmetries in plasma characteristics. It was suggested that the ExB drift is the likely cause. It has the right direction, the right order of magnitude, and the right dependence on density, through the electron temperature at the plate. The effects of imbalanced radiation, detailed in that paper [14], enhance

the power imbalance, and should account for the final observed state. Other potential causes, such as thermoelectric currents are not ruled out but are not needed.

IV. Effect of drifts on the divertor plasma

The question of drifts also was addressed with respect to the divertor itself. The private flux zone (PFZ) is often neglected in discussions of the divertor. But, it could potentially be playing an important role in neutral compression, detachment, and the flow of plasma between outer and inner divertor (or vice versa). What is least understood about the PFZ is why there is much plasma there at all given the short connection lengths from x-point to divertor plate and typical diffusive transport. Using spectroscopic measurements, it was observed that there is a significant recombination rate in the PFZ [17]; Up to 10^{22} recombinations/s occur there as compared to the plate ion current which can reach ~ $5x10^{22}$/s for these plasma currents (see Section IX). A drift across the outer divertor leg (between x-point and divertor plate) was postulated as the mechanism to supply the corresponding ion current to the PFZ. The drift is due to a poloidal temperature gradient along the separatrix from the x-point to the outer divertor plate (thus an electric field) which generates an ExB flux into the PFZ from the common flux region of the outer divertor.

The temperature-gradient driven ExB flux into the PFZ is approximately linearly dependent on pressure and logarithmic with respect to the ratio of the x-point temperature, T_x, to the temperature at the divertor strike point, T_{sp} [17]:

$$I_e \approx \frac{1.42 \cdot \pi \cdot R^2 p_e}{e B_0 R_0} \ln\left(\frac{T_x}{T_{sp}}\right) \quad (1)$$

where R_0 and B_0 are the major radius and magnetic field at the plasma center. In cases where the outer divertor is attached the pressure, p_e, is constant along the separatrix. As the outer divertor

approaches detachment the PFZ region recombination rate increases as the temperature at the strike point drops (increasing T_x/T_p). Since recombination is the primary sink for ions in the PFZ the flux into the PFZ is approximated by the integrated recombination rate. One can then compare Eq. 1 with the total recombination rate integrated over the PFZ derived from D_γ (see Figure 6).

As the line averaged density is increased further, the outer divertor leg becomes detached and a region of constant low-temperature ($\leq$ 1 eV) extends from the divertor plate up to the detachment front, a short distance below the x-point. This results in a poloidal temperature drop over a shorter distance. Thus the flow into the PFZ is restricted to a region slightly below the x-point, reducing the flow into the PFZ due to the aforementioned drift. Those points are also included in Figure 6 but now using the maximum pressure along the separatrix below the x-point. As the density is increased still further and the detachment moves to the x-point plasma flows from the Common flux plasma to the x-point due to the local temperature gradient. This cools the plasma on closed flux surfaces enough to help drive an x-point MARFE, which can subsequently lead to a disruption.

V. High recycling vs. detached divertor operation

C-Mod divertor operation can be described as 'dissipative' over most of its operating space. By dissipative we mean that $0.5xP_{SOL} \leq P_{rad,Div} \leq P_{SOL}$ where P_{SOL} is the power flowing into the SOL across the separatrix and $P_{rad,Div}$ is the radiated power in the divertor region (but outside the separatrix).

The C-Mod divertor is required to dissipate higher parallel power flows than other tokamaks, more towards the level of a Burning Plasma Experiment (BPX) like ITER.[18] This is due to the high toroidal magnetic field and the accompanying high plasma current density. Even

in ohmic 1 MA plasmas the parallel power flow, $q_{||}$, is of order 200 MW/m^2, rising to > 500 MW/m^2 or more during high power heating [19]. Figure 7 is an example of the parallel heat flux profile. This is to be compared to predictions for ITER which are of order $q_{||}$ = 1000 MW/m^2.[20] Other tokamaks are typically factors of 2-3 lower in $q_{||}$ than C-Mod for high-power shots.

The characteristics of the divertor radiation, where it occurs in the divertor and the radiating species, vary as the divertor plasma changes from high-recycling to detached. The C-Mod group was one of the developers of bolometric tomography in that region. As early as 1994 multiple bolometer viewing chords were brought to bear on the divertor giving an integral of the radiated power from that region [21]. They were quickly followed by more viewing chords (e.g. see Figure 2b) and tomographic inversions of the bolometer brightnesses to obtain local emissivities [22]. (The number of bolometer arrays focused just on the divertor was later increased to 5 [19]). Examples of both the result of tomographic inversions of divertor bolometer data and the variation in emissivity are shown in Figure 8. During high-recycling operation, the largest emissivity is located near the inner divertor. There is also significant emissivity spread along the outer divertor leg of the separatrix. For this Ohmic plasma, the peak in the emissivity has a value of < 30 MW/m^3. During an ICRF-heated (P_{RF}=2 MW) high-recycling discharge, the peak in the emissivity reaches a value of 60 MW/m^3, with large regions having emissivities of >10 MW/m^3. The largest emissivity is located on the inboard side only when the ion ∇B drift is directed toward the divertor. If the ion ∇B drift is directed away from the divertor, the largest emissivity is located near the outer divertor plate [14]. As the divertor plasma becomes detached, the peak in the divertor emissivity moves away from the divertor plate towards the x-point, and finally inside the LCFS near the X point (see Fig. 8b). This movement can be rapid (≤10 ms) or gradual (≥100 ms) depending on how quickly the temperature in the divertor is evolving. It is well correlated with the decrease in the ion saturation current collected by probes embedded in the divertor

plates. The peak values of the emissivity are very similar to those measured in the high recycling divertor regime. Goetz [22] divided the radiation measured by the divertor bolometer tomography into two parts – $P_{rad,div,in}$ and $P_{rad,div,out}$, the fraction emitted from inside and outside the separatrix respectively. Thus the total core plasma radiation can be determined as $P_{rad,inLCFS} \equiv P_{rad,div,in} + P_{rad,main}$. The latter is the poloidally symmetric radiation from inside the separatrix determined from a toroidally-viewing bolometer array at the midplane. When the divertor detaches, the total power losses inside the separatrix , $P_{rad,inLCFS}$, become larger than those in the divertor region outside the separatrix due to the spatial movement of the divertor volumetric losses and a slight increase in the main plasma radiated power. Also, the ratio of $P_{rad,div,out}$ to $P_{rad,div,in}$ changes from a value of about 3 to about 1 as the divertor plasma goes from the high-recycling to the detached divertor regime.

The ratio of divertor radiation, $P_{rad,div,out}$, to radiation inside the separatrix, $P_{rad,inLCFS}$, changes as the divertor transitions from high-recycling to detached[22]. In high-recycling plasmas the divertor radiates almost as much power as the much larger core plasma (see Figure 9). This is due to the very high local divertor emissivities as already discussed. When the divertor detaches and radiation moves to the region of the x-point, more radiation occurs inside the separatrix and less radiation originates from the divertor. Thus the transition to detachment degrades the dissipative nature of the divertor.

From the point of view of limiting the flow of ion power to the divertor plate, the detached plasma still has advantages. Figure 10 shows a high power L-mode discharge with both Ohmic and high-power L-mode phases. Detachment is first induced by puffing methane gas into the divertor and increasing radiation there [22]. The electron pressure the plates drops as the transition is made from high-recycling to detached divertor twice (one probe location shown in Fig. 10d).

The corresponding heat flux is dropped further as it is proportional to the $n_e T_e^{1.5}$ (T_e has also dropped).

Further illustration of the effect of detachment on the power flux to the divertor plates is shown in Fig. 11 [22]. Although both the high recycling and detached divertor operational regimes severely limit the power reaching the plates, the detached divertor generally has lower power fluxes.

The movement of a significant amount of radiation from the divertor across the separatrix to the main plasma is symptomatic of another difference between high-recycling and detached operational regimes. There is a detachment 'front' typically between the x-point and the outer divertor. This means that there are large parts of the divertor, between the detachment front and the divertor plates, which are low density (e.g. $10^{19} – 10^{20}$ m^{-3}) and low temperature (≤ 1 eV) contributing little to radiation losses. The particle flux to the divertor plate has dropped, often by factors of 10-100. The impurity source rate due to physical sputtering has dropped (drop in ion flux and T_e). This is good from the point of view of divertor lifetime. On the other hand the divertor plasma has become much less opaque to low-Z impurities such as He, C and N [23]. Thus the screening of impurities from the core has been degraded.

In summary, high recycling operation is in general quite good. Due to the high densities in C-Mod the divertor radiation can be quite high, reducing the heat load on the plates. The transition to detachment reduces the power flow to the divertor plates even more than for the high-recycling divertor with the additional advantage of reducing the particle flux, resultant divertor erosion, and impurity influx. The disadvantage of detachment is the reduction in impurity screening and the concomitant cooling of the plasma inside the separatrix.

VI. General detachment characteristics

The initial observations of detachment at C-Mod evidenced a large decrease in ion saturation current at the divertor plates. An example is shown in Figure 12. As the line-averaged density is increased (or plasma current decreased) the ion saturation current collected by probes embedded in the divertor plate initially increases. At the detachment transition (~0.72 sec) an abrupt transition from standard radiative divertor to detached divertor occurs. The ion saturation currents on the outer divertor probes exhibit a rapid change or rearrangement. The separatrix strike point is between outer divertor probes 5 and 6 (see Fig. 2a for locations of probes). At probes 1 through 7, which are located below the nose (location of probe 8 in Fig. 2a) of the outer divertor, I_{SAT} drops. The opposite is true at probe locations at and above the nose (probes 8-10).

There are a number of other characteristics, both in the edge and central plasmas that are affected by the transition to detached divertor operation. At detachment, the time-derivative of the line-averaged density increases for a fixed gas-puff rate. We interpret this as poorer screening of neutrals from crossing the separatrix into the core plasmas. A similar effect is often observed in the behavior of the midplane neutral pressure measurement as that is strongly linked to the core density. The absolute magnitude of the divertor radiation does not change significantly although the concentration moves from the region near the outer divertor plate to the region of the x-point (Section V). A large fraction of this x-point radiation is actually inside the separatrix (see section V). Accompanying the change in particle flux to the divertor plate are abrupt decreases in the density and temperature at the divertor plate. Figure 13 shows those parameters from one Langmuir probe at the outer divertor plate surface (probe 7) for a typical scan of density for Ohmic plasmas. The probe flux surface location was in the range ρ =1-4 mm, the distance outside the separatrix, referenced to the midplane. The dependence on $\bar{n}_e/I_p$ is because either a density increase or a current decrease can bring on the scaling seen. As the core density is increased, the density at this point on the divertor plate increases non-linearly, a high-recycling condition.

Simultaneously, T_e drops in such a way to keep the pressure constant along the flux surface as measured by a probe upstream (section II [24]). When the divertor T_e reaches ~ 5 eV, the local density abruptly drops by an order of magnitude or so. This, of course, corresponds to the drop in particle flux to the plate described earlier. Once past the detachment threshold $T_{e,plate}$ appears to stay around 1 eV. It is probable that such probe-derived temperatures are higher than they should be due to kinetic effects [25]. In fact, as discussed below, spectroscopic measurements of density and temperature away from the plate after detachment show that even lower temperatures can be found in the detachment region, ~ 0.4 eV.

The drop in current to the divertor plates was postulated by Stangeby [26] to be due to pressure loss along the flux surface between the region outside the divertor and the plate. This was verified through a number of measurements on C-Mod. Shown in Fig. 14 is an example where the electron pressure upstream as measured by the scanning Langmuir probe (located just outside the divertor) is compared to the electron pressure at the plate. The ratio of upstream to downstream pressures, f_m, is given for a number of discharges and on several flux surfaces outside the separatrix. At points above the divertor nose there is no pressure loss (f_m ~1) as discussed earlier. In some cases it was found that just prior to detachment (T_t ~ 10 eV) the pressure in the ρ=2 mm region of the plate actually rose compared to regions outside the divertor (f_m ~ 2-3). This phenomenon was termed a 'death ray' because it was concentrated a high heat flux into a very narrow region of flux space, leading to increased power fluxes there [16]. This behavior suggested a mechanism of parallel momentum *increase* in flux tubes adjacent to the flux tubes connecting to the detached region, perhaps involving momentum exchange between strong parallel plasma flows there via charge-exchange neutral transport.

Given that the detachment process was predicated on neutral-ion collisions removing ion momentum, the C-Mod group made several attempts to infer the neutral density in the detachment region. Utilizing localized D_α measurements and the plate probe-derived plasma characteristics, the local neutral D atom density was derived [27,16]. Based on this analysis, it was

noted that the neutral density was more than enough to account for the momentum loss observed during detachment. This analysis was taken one step further by utilizing a tomographic inversion technique [27], together with the plasma characteristics at the plate, to derive the neutral atom density along the plate. This showed that there should be more pressure loss than measured experimentally *if* the neutrals were at rest. The implication was that the neutrals were moving at close to the background plasma flow velocity (sound speed at the plate) and thus did not remove as much momentum as stationary neutrals could. Later flow measurements appeared to confirm this [28].

The development of tomography of C-Mod CCD camera images filtered for D_γ [17] confirmed that the low-temperature detachment region extends far from the divertor plates. In the sequence of reconstructions shown in Fig. 15, the density is increasing as a function of time. As the density is raised the peak in D_γ emission increases and moves away from the divertor plate towards the x-point. The plasma detaches between 0.6 and 0.7 seconds. In its final state, the D_γ emission is peaked on those flux surfaces that impact on the divertor plate below the divertor 'nose' and extends to the x-point; The extent of the detached region in ρ space, as determined by the D_γ tomography, is consistent with that determined by probe measurements at the plate. The detachment front, or the demarcation between the high density recombining plasma and the detached plasma, is at the peak of the D_γ emission. As described in section IX, spectroscopic measurements of the high-n Balmer series emissions indicate that the peak in D_γ emission is where the density is highest.

While the divertor bolometry is able to determine the local emissivity and total power loss from the divertor region, it is still of interest to understand the makeup of that power loss. An extreme-ultraviolet (XUV) spectrograph and a visible spectrograph have been used to survey the

radiation (as opposed to neutral losses) coming from the divertor region . For these studies, the X point had been shifted to larger major radius and up vertically to be in the field of view of the XUV spectrograph. These studies [22] show that the total radiation emissivity is dominated by XUV radiation. For plasmas with low central density (sheath-limited, $\bar{n}_e \sim 1\text{x}10^{20}\ \text{m}^{-3}$), the significant contributors to the observed radiation in the XUV wavelength range of 6– 116 nm were argon, fluorine, carbon, and oxygen These measurements were made before any boronization. After boronization, boron radiation replaced that from carbon and oxygen. Argon is normally puffed in trace amounts to perform core ion temperature measurements, while the other three are intrinsic impurities. At these low densities D^0 emission accounts for roughly 7% of the total radiative loss measured by the bolometer array. The XUV radiation accounted for ~ 50% of the radiation measured by the bolometer array (with large error bars [22]). As the central density is raised, the divertor enters the high-recycling divertor regime. In this regime the contributions of D^0 line radiation and continuum emission (assumed to be bremsstrahlung) are close to 10%, while the XUV contribution was close to 25%. The inference of these results was that neutrals must be accounting for the remainder of the power losses measured by the bolometer arrays, of order 50-60%. In all Ohmic plasmas, molybdenum is a negligible contributor to the XUV and visible radiated power in the divertor.

The role of neutrals in divertor power loss was later investigated more directly using a diagnostic developed at C-Mod [29]. Since the bolometers are sensitive to neutrals as well as radiation, a neutral ‘filter’ was created by injecting neutral D_2 or He into the bolometer camera housing to raise the pressure there to ~ 200 mTorr. At such pressures the mean free path for small-angle scattering (a few mm) is much shorter than the distance a neutral must travel through the high-pressure region to reach the bolometer foils and be absorbed (~4 cm). This technique

was used to study a set of 3 ICRF-heated detached L-mode discharges which are shown in Fig. 16; two discharges have neutral filtering starting at ~0.5 seconds, one discharge without filtering (solid line). The divertor plasma is detached during the filtering period except for when the ICRF power is on (attached). The neutral power loss component remains at a fairly constant fraction (~30%) of the total integrated emission through both ohmic detached, and partially reattached periods. The neutral emission is peaked on bolometer chords aimed in the vicinity of the x-point or below. Unfortunately, the same XUV study of the makeup of radiation was not repeated in parallel with the neutral power investigation. In either case the indication is that neutrals are playing a significant role in power losses from the divertor, in the range 30-50% of the total divertor losses for both detached and high-recycling divertor conditions. In addition, one must be concerned as divertors become more dense and larger such that charge exchange neutrals, emitted by the plasma, can be absorbed before reaching the bolometer detectors outside the plasma. This will lead to difficulties in obtaining the local emissivity for obvious reasons.

When the density is raised far past the detachment threshold the bolometer and Dγ tomography both shows that the radiation moves out of the divertor proper to regions at, or above, the x-point. There are two recombination regions, one in the divertor and a second INSIDE the separatrix, reaching up to 4 cm above the x-point. The corresponding midplane location for this region is 0.4 cm inside the separatrix. The recombination-dominated character of this 'x-point MARFE' is very similar to that identified for the MARFE at the inner midplane [29].

The existence of a second cold and dense recombining region inside the separatrix leads to effects on core radiation and the core T_e profile. This is verified by the time behavior of the principal VUV line intensities (O, N, D) for a spectrograph viewing chord passing through the upper edge of the x-point MARFE[29,30]. The sequential peaking and drop of successively lower-

energy charge states of N and D imply that the local T_e is dropping precipitously from ~ 50-70 eV -> ~5 eV. The plasma above the x-point becomes so cold that D^0 line radiation is dominant. An ECE measurement of T_e 2 cm inside the separatrix at the midplane mirrors this cooling effect. The discharge terminates when the x-point MARFE moves from the x-point to the inner wall and spreads poloidally. All of this occurs at a density corresponding to ~60% of the Greenwald limit [31] whereas the detachment threshold typically occurs at 30% of the density limit.

VII. Detachment threshold and its modification (n_e, ICRF, geometry)

Experiments were undertaken on the Alcator C-Mod tokamak to modify the onset density and other characteristics of divertor detachment. In general $T_{e,plate} < 5$ eV has been shown to be a controlling factor in the detachment onset [26,21,32,16]. Using simple 1D fluid SOL heat transport ('2-point') models [33,16,34] one can write down a relationship between the plasma parameters and the power flowing in the SOL, $q_{\parallel}$. Assuming that radiation losses occur along a flux surface only in the region from the x-point to the plate, we define $f_{loss,}$ the fraction of parallel heat flux lost to radiation, charge-exchange and ionization of neutrals [35] by:

$$q_{\parallel,x}(1 - f_{loss}) \equiv q_{\parallel,plate} \tag{2}$$

$q_{\parallel,x}$ and $q_{\parallel,plate}$ are the parallel power flow into the divertor region (from the SOL) and to the plate respectively. Further assuming that pressure is constant on a flux surface, one can then solve the heat transport equation for the dependence of $T_{e,plate}$ on the connection length, L, upstream and core parameters:

$$T_{plate} \propto \frac{q_{\parallel,x}^{10/7}(1 - f_{loss})^2}{L^{4/7} n_{upstream}^2} \tag{3}$$

This can also be written in terms of general SOL plasmas:

$$T_{Plate} \propto \frac{P_{SOL}^{10/7}(1 - f_{rad,global})^2}{L^{4/7}\lambda_{q\|}^{10/7} n_{upstream}^2} \quad (4)$$

where $f_{rad,global} \equiv P_{rad,div}/P_{SOL}$ is the fraction of power flowing into the SOL that is lost to radiation before reaching the plate, $\lambda_{q\|}$ is the radial e-folding length for the parallel heat flux in the upstream SOL, and $n_{upstream}$ is the upstream SOL density. Equation 4 confirms the three primary avenues to controlling T_{Plate} and thus detachment: (1) increasing the core plasma density ($n_{upstream}$); (2) decreasing $q_{\|}$ (P_{SOL}); and (3) increasing $P_{rad,div}$ ($f_{rad,global}$).

Neon has been found to be effective in reducing the detachment onset density in Ohmic plasmas. The results of such experiments are shown in Fig. 17 for 800 kA discharges with $\bar{n}_e$ increasing throughout the pulse. Neon was injected in varying amounts early in the discharge leading to a variation in the detachment onset density. The detachment onset density could be decreased by almost a factor of 2. The Ne injection is not without adverse effects; Z_{eff} and radiation in the core plasma both increased ($\Delta Z_{eff} < 0.8$) due to the increase in impurity penetration that accompanies detachment. Experiments with Ohmic plasmas have shown N_2 and CD_4 to be similarly useful in bringing about detachment. The primary advantage of these lower Z gases over Ne/Ar are: (1) more radiation is in the divertor region; and (2) the increase in core radiation is minimal before detachment [23].

Increased radiative losses reduce the power flow to the divertor and thus can reduce the detachment onset density. Experiments have also been carried out to determine the usefulness of adding power flow to control detachment *without* addition of extrinsic impurities. For the Ohmic plasmas discussed above, the core energy confinement can be characterized as L-mode. Fig. 18a-c shows the effect of increasing the power flow into the SOL, through ICRF heating, for an

already detached divertor plasma. Shown in this figure are the divertor characteristics at three different flux surfaces in the SOL; ρ = 0, 2 and 4 mm (not detached) in distance from the separatrix.

The divertor plasma characteristics shift towards reattachment as P_{SOL} is increased. When T_e at ρ = 2 mm reaches ~ 5 eV the corresponding density peaks and starts to decrease as the separatrix density continues to rise. Even for an increase in P_{SOL} of a factor of 5, the pressure is still not peaked at the separatrix (ρ = 0 mm). This corresponds to $T_{e,separatrix}$ (ρ = 0) still not reaching the detachment threshold of ~5eV.

Radiation in the divertor is counteracting much of the effect of increasing P_{SOL}, Fig. 18d. It is apparent that as P_{SOL} is increased, $P_{rad,div,out}$ increases at a slower rate (see the description of Figure 9 for an explanation of $P_{rad,div,out}$). Shown for comparison is a line corresponding to $P_{rad,div,out} = P_{SOL}$. Note that as P_{SOL} increases above ~ 0.6 MW, the divertor radiation peak has moved back outside the separatrix as evidenced by the decrease in $P_{rad,div,in}$. This movement corresponds to increases in $T_{e,plate}$.

While the above description of the detachment process and accompanying plasma characteristics is primarily using examples of L-mode plasmas, the characteristics of detachment are similar for H-mode plasmas: location of the detachment front, low pressure and heat flux at the plate. The primary difference for H-mode plasmas lies in the detachment threshold. As the power injected rises, certainly the threshold should increase as discussed in this section. In addition, the power e-folding length in the SOL, λ_q, decreases roughly by a factor of 2, leading to higher power densities (see Eq. 4). These two effects significantly increase the difficulty of achieving detachment. Lastly, in H-mode the core density can double while the SOL density and the divertor density change little. All these effects lead to an increase in the measured

detachment threshold as can be seen in Figure 19 [19]. The plasma transitions to H-mode at 0.6 seconds. The density rises and the divertor is not detached even for Greenwald fractions of 0.55, almost a factor of 2 greater than for Ohmic plasmas. This figure also shows the results of an impurity injection system which uses feedback on the bolometer chord through the x-point to control the rate of N_2 into the divertor (shown in Fig. 19g) to increase f_{Rad}. The nitrogen radiation builds up both in the divertor (shown in ref [19]) and the core (Fig. 19c). Such impurity injection is required to compensate the high power and decrease in λ_q. Detachment occurs at 0.8 seconds when the pressure at the plate drops to zero [19]. The feedback senses the x-point radiation rising too much (detachment front moving towards the x-point) at which time the N_2 gas feed is throttled back to achieve a steady state for the remainder of the shot. As can be seen there is some degradation of core confinement and increase in radiation. The Greenwald fraction also rises to ~ 0.7. Other impurities were also tried on C-Mod. It was found that Ar and Ne place too much radiation in the H-mode pedestal, and less in the divertor compared to N_2, thus degrading core plasma performance over that obtained with N_2 [19].

Another significant difference between L- and H-mode detachment is the magnitude and role of recombination. The C-Mod experience shows that detached H-mode plasmas have little or no recombination compared to L-mode detachment. Section IX has much more detail about recombination.

It is sobering to contemplate the implications of the above impurity feedback experience for an ITER-like device. In that case the parallel power flux is predicted to be double that of C-Mod, making it even more difficult to detach. The details of actual, as opposed to predicted, power widths, the appropriate impurity to inject, and how the injected impurity will affect core performance (what fraction crosses the separatrix) are still to be settled, and we will likely not be

sure until ITER is built and operated.

VIII. Effect of geometry on detachment

Soon after the characterization of detachment on C-Mod had begun, it became clear that the Ohmic detachment threshold was lower on C-Mod ($n_{e,detach} \sim n_{Greenwald}/3$) [21]than all other tokamaks ($n_{e,detach} \sim n_{Greenwald}/2$).[32]. Experiments were started on C-Mod to determine whether this was an effect of vertical-plate divertor geometry or of the higher density, both unique at that time. The conclusion was that geometry is the primary factor.

Three types of divertor geometries compatible with operation were developed for C-Mod and are shown in Fig. 20. By varying the outer divertor strike point position the divertor geometry is effectively changed from 'vertical-plate' (a) to 'slot' (b) to 'flat-plate' or 'open' divertor (c). The inner strike point was always below that divertor's 'nose' and the inner divertor plasma was always detached for the discharges described in this section.

A density scan was performed for the same plasma core conditions and for each of the different divertor geometries shown in Fig. 20. Detachment on a given flux tube is determined by examining the ratio of electron stagnation pressure at the target to that upstream in the SOL, $2n_eT_{e,plate}/n_eT_{e,SOL}$. When this ratio falls below 0.5 on a given flux tube then that flux tube is considered to be detached. The extent of detachment, ρ_{detach}, is shown in Fig. 21. ρ_{detach} is then the distance from the separatrix to the first attached flux tube referenced to the midplane. For the standard vertical-plate geometry, the detachment extent abruptly increases at $\bar{n}_e \sim 0.3 x n_{Greenwald}$, such that the divertor pressure deficit reaches the flux surfaces that intersect the juncture between the vertical and semi-horizontal sections of the outer divertor plate (herein designated the 'nose' of the outer divertor, 'N' in fig. 20). The detachment extent does not increase beyond the divertor

nose even for densities 2.5 x the detachment threshold. The differences between vertical-plate and slot operation are minimal in the onset of detachment. As in the case for the vertical plate geometry, the extent of detachment for the slot divertor geometry increases till ρ_{detach} corresponds to the divertor nose. In the slot divertor case this means a larger fraction of the common flux zone is detached.

The detachment threshold for the flat-plate geometry is much higher than for the vertical or slot divertor geometries. $N_{detach} \sim 0.5 x n_{Greenwald}$, as expected from the experience of open divertor tokamaks. In addition, the pressure deficit at the plate is typically smaller ($2n_eT_{e,plate}/n_eT_{e,SOL}$ ~ 0.1 compared to .01 for vertical-plate). Lastly, the detachment occurs above the nose, where for the other two geometries, the divertor nose was the limit.

Because the midplane pressures for all configurations track as a function of density independent of detachment, the flat-plate divertor has higher midplane pressure at detachment then slot- and vertical-plate geometries. The core Z_{eff} is the same for all three geometries. But surprisingly, the divertor neutral pressure is also approximately the same when the divertor geometry changes from the pressure measurement plenum being in the private flux region (vertical-plate) to sampling the common flux region (slot). More information about this appears in the companion C-Mod paper on neutral physics [36].

The variation of the plasma characteristics at the plate evidence both similarities and differences among the three types of detached plasmas. Unfortunately there were no Langmuir probes in the region of the strike point for the slot divertor plasma. Figure 22 shows the temperature at the plate on the ρ=2 mm flux surface and the upstream SOL T_e (vs $\bar{n}_e$) for both vertical and flat-plate divertor plasmas. As $\bar{n}_e$ is increased we see that $T_{e,plate}$ for the two divertor plasmas tracks from a sheath-limited condition into a high recycling mode. When $T_{e,plate}$ drops to

~ 5eV there is a subsequent abrupt drop to 1-2 eV, the density threshold being consistent with Fig. 21. However, the vertical-plate plasma T_e separates from that for the flat-plate at densities lower than the detachment threshold, likely indicating a transition to a high-recycling condition earlier.

Equation 4 can be used to infer the reasons for the differences in detachment threshold for the various divertor configurations. $q_{||}$ is independent of geometry. Because $T_{e,plate}$ is essentially the same for all divertor geometries, we can expect from Eq. 4 that $\bar{n}_{e,detach} \propto q_{||,x}^{5/7}(1-f_{loss})L^{-2/7}$. The dependence on L is too weak (~20% variation among the various geometries) to explain the threshold variation among the various geometries. The parallel power flow appears to be essentially the same among them as well (as can be derived form the upstream T_e in Fig. 22). Thus it is possible that there is a variation in f_{loss} with configuration which would lead to differences in detachment threshold.

One obvious difference brought about by the geometry changes is that the parallel field line length *in the divertor* is varied. We define this 'divertor connection length', $L_{x,connect}$, to be the distance along a field line (ρ = 2 mm flux surface) from the separatrix intersection with the outer divertor plate (strike point) to a horizontal plane located at the x-point (see Fig. 23b). In a series of discharges the strike point was moved to different locations along the outer divertor plate creating equilibria varying from slot to flat-plate. The resultant detachment onset densities are plotted vs. the divertor connection length in figure 23a. The corresponding location of the outer divertor strike point is also shown for each case.

The combination of f_{loss} (inferred) and $L_{x,connect}$ (property of the geometry/equilibria) imply that the changes in geometry from flat-plate to vertical-plate bring on changes in losses along a flux surface. The discussion of reference [37] indicates that the vertical-plate geometry has a longer

low-T_e, and thus radiating, region below the divertor nose than the flat-plate geometry has above the nose. This could be due to the geometry itself whereby recycling neutrals are aimed back at the separatrix for all points below the nose, as opposed to points above. Such high recycling allows increases in density and decreases in temperature along the field line both of which engender higher radiation.

The neutral density in the plasma fan in the region near the plate may also have an effect on detachment. It was shown [27] that the neutral density above the nose is lower than for the vertical plate region. One might expect this because neutrals created above the nose can easily be 'pumped' by the core plasma or lost towards the lower pressure midplane. Neutrals created on the vertical plate are accumulated in the divertor and have trouble escaping.

IX. Recombination and ion loss

The initial analysis of detachment led researchers to conclude that the loss of current to the divertor plates could be due to ion-neutral momentum losses (e.g.[26,21,32]). The loss of ions due to recombination was not thought to be important because divertor temperatures were too high, perhaps near 5 eV. As more divertor data was acquired it became apparent that the last assumption was not true. The lowest probe measurements of divertor T_e were $\leq$ 1 eV (see Figure 14) on Alcator C-Mod [24,21]. This spurred researchers to postulate that not only did recombination occur, but it *must* occur [38-40] (see Figure 14). The first experimental measurements of significant volume recombination in a tokamak divertor were made on Alcator C-Mod [41] where quantitative evidence was found in the emission spectrum of D^0. After this initial C-Mod measurement, the existence of recombination was confirmed at other tokamaks [42-44]. Unfortunately, because of the difficulty of interpreting the D^0 spectra, most of the initial measurements from other tokamaks were limited to the 'signature' of recombination, namely the ratio of brightnesses from different

D^0 lines (e.g. Ly_β/Ly_α [45] or D_γ/D_α [43]) which drops precipitously when recombination occurs.

The first step taken in determining the recombination rate was to develop a formalism for quantitative analysis [41,46]. This formalism applied only to three-body and radiative recombination. As an aside, there is a third path to recombination, involving molecules via Molecular Activated Recombination (MAR). MAR has generally been found to be low in tokamaks. The C-Mod research on this topic is contained in [46]. Returning to three-body recombination, a distinction is made between those recombinations that end with an atom in the ground state, called 'complete' recombinations, and those where the atom is re-ionized before the ground state is reached. Only 'complete' recombinations will be significant in the ionization/recombination balance in tokamaks and a measure of their rate was the goal of the analysis. The formalism could be used to interpret measurements of the Balmer and Lyman series lines of D^0. Because the Balmer lines occur in the visible and the Lyman lines appear in the vacuum ultraviolet, the spatial coverage of Balmer series measurements is much more extensive and they were thus primary diagnostic for recombination measurements.

The above techniques were further developed to make it easier for the recombination rate to be determined by the spectroscopic measurement of one emission line (e.g. D_α) [46]. Three-body 'complete' recombination occurs dominantly by recombination into excited states that decay radiatively to the ground state. Thus, if three-body recombination is the only process populating the atomic excited states, measurement of the total number of radiative decays to the ground state per unit time is a direct measure of ~90% of the total recombination rate, excluding MAR. (The last ~10% of the 'complete' recombinations occur by collisional de-excitation and by radiative recombination directly into the ground state.) Recombination tends to populate the high-*n* levels (in a Saha–Boltzmann distribution). Using a Collisional-Radiative (CR) model the number of

recombinations per emitted photon was detailed [46] in an analogous fashion to what Johnson and Hinnov [47] did in the *ionizing* case. The CR model in the *recombining* case yields the temperature and density dependence of the number of 'recombinations per photon' for the D^0 lines. An example of this quantity for $D\gamma$ vs T_e is shown as the top, solid line in Fig. 24 under the assumption that the divertor plasma is optically-thin for the Lyman series lines. Figure 24 also shows the effect of hydrogen Lyman series line radiation trapping (discussed later).

It is clear from an examination of Figure 24 that the local electron temperature can be important, especially in the case for which Ly_α is optically thick, in determining the recombination rate. Initial expectations were that T_e in the recombining region were no lower than that measured by probes at the divertor plate, $T_e \sim 1$ eV. This placed the estimated recombination rate in a 'flat' region of the recombinations per photon curve. However, more direct measurements of T_e (and n_e) in the recombining region were warranted.

The Balmer and Lyman series spectral emission provided such a measure of the characteristics of the recombining plasma (Fig. 25a, b). Such characteristics are an average over any recombining region within the viewing chords but clearly, given that the recombination rate $\propto n_e^3$, the weighting is to the strongest recombining regions. The high-p ($p \geq 4$, where we substitute 'p' for the more standard 'n' to distinguish from density) Balmer lines are significantly broadened compared to the instrumental width of the instrument used for this C-Mod study. A Voigt profile was fit to the data to obtain the FWHM of the $p=6,7,8,9 \rightarrow 2$ lines (Figure 25c). Using standard Stark analysis techniques (e.g. Ref. [48]), the density in the recombining region is determined from the $p=6,7,8,9 \rightarrow 2$ lines with typical uncertainties of 2-3 x 10^{20} m^{-3}.

The Balmer spectrum can also be used to determine the temperature in the recombining region. The population densities of excited states, when dominated by recombination ($T_e \leq 1$ eV)

should scale according to the Saha-Boltzmann distribution:

$$n_p \propto \frac{p^2}{T_e^{3/2}} \exp\left(\frac{13.605}{T_e p^2}\right) \qquad (5)$$

where $(13.605/p^2)$ is the ionization energy for the pth level. The population densities of the p=5 through 8 → 2 lines are fit to Eq. 5 (Fig. 25d) to obtain T_e (neglecting the p=9 and 10 → 2 lines due to their overlap as well as their large 'wings', which are difficult to fit). The inferred T_es are found to be in the range from 0.4 to 0.8 eV [30]. The uncertainties of this measurement are related to the possible modification of population densities by the opacity of the plasma to $Ly_{\alpha,\beta}$ or by excitation from the ground state and were estimated to be ~±0.1 eV.

The above techniques for inferring the local n_e and T_e allowed the evolution of the outer divertor plasma to be studied from a perspective not limited by the probes embedded in the plates themselves. The detachment region appears to form in the Private Flux Zone (section IV) before forming on the other side of the separatrix in the Common Flux Zone (CFZ). Then as the density is increased, the detached CFZ region, corresponding to the peak in the Stark-derived density moves from the strike point up the divertor plate. This measurement correlates with the movement of the D_γ emission peak as observed by D_γ tomography [30,17] (see Figure 15).

Given the measurement of the density and temperature in the recombining region, the Dγ brightnesses can be used to determine more accurately the total recombination rate using the recombinations per photon of Fig. 24. The detailed profiles of the chordal integrals of recombination are for views spanning the divertor region then summed to obtain the total recombination sink (I_R) affecting each divertor plate. A corresponding spatial integration of probe ion saturation current over the divertor surfaces is used to determine the divertor plate ion sink, I_P. The total ion sink is then:

$$I_S = I_R + I_P \quad (6)$$

where the integration to obtain I_R does not include recombination inside the separatrix. The outer divertor integrals giving $I_{S,R,P}$ are displayed in Fig. 26(a). The current to the region of the outer divertor plate below the nose, I_P, starts decreasing at ~0.73 seconds, ultimately dropping to ~25% of its peak level. The local drop in ion current can be larger (≥10 near the separatrix) and is simultaneous with local drops in pressure both of which start at ~0.6 seconds, before the ion current integral over the divertor, I_P, drops. Recombination (I_R) increases before detachment **and** before any clear reduction in I_P. In addition, the I_R increase during the discharge is not equal to the drop in I_P. Thus the total *inferred* ion source, equal to I_S, decreases during detachment. By the end of these detached, Ohmic L-mode, plasma discharges most ions (~75%) created in the divertor recombine before reaching the divertor plate. If we have underestimated the recombination rate (based on our assumptions of constant opacity throughout the divertor region) then an even larger fraction of ions (~90%) would recombine before reaching the plate.

Based on a 'two-point' model (*e.g.* [49]) for **attached** plasmas one expects the total ion sink (ion source) to scale as $n_e^2 / P_{SOL}^{3/7}$, where n_e is the density upstream in the SOL and P_{SOL} is the power crossing the separatrix into the SOL. For reference we display the attached ion source scaling in Fig. 26(b) utilizing the line-averaged density, $\bar{n}_e$ (roughly proportional to the upstream density) for this almost constant P_{SOL} shot. The difference between the inferred ion source in detachment and that predicted for attached plasmas indicates that the occurrence of detachment reduces the ion source relative to the attached case. This concept is also known as the 'degree of detachment'[12].

The relative magnitudes of the plate and recombination ion sinks vary with plasma current and input power. In Fig. 27 we see that as expected, the plate current peaks, and then falls as $\bar{n}_e$ is increased past the detachment threshold ($\bar{n}_e$=1.7x10^{20}m^{-3} for 0.8 MA, =2.3x10^{20}m^{-3} for 1 MA). The higher plate current and detachment threshold for 1 MA Ohmic plasmas is simply due to the higher power flowing into the SOL and divertor (Section VII). The story is more complicated for I_R. I_R (only the recombination outside the separatrix) increases linearly through detachment until I_P starts to asymptote to a minimum for both 0.8 and 1.0 MA discharges. The 0.8 MA discharges are then characterized by a saturation in the recombination level as the x-point MARFE begins forming ($\bar{n}_e$=2.5x10^{20}m^{-3}), substantial recombination occurs inside the separatrix, and $\bar{n}_e$ is further increased. At the highest densities, $\bar{n}_e \geq 3.5\text{x}10^{20}\text{m}^{-3}$, the x-point MARFE is just beginning to form in 1 MA discharges and there is no obvious saturation of I_R in that case.

The addition of core heating affects the relative balance of ion sources and sinks in the divertor. When the ICRF heating waves were injected into an already detached discharge the recombination ion sink stays constant but the plate ion current increases [30]. The inference is that the ion source is increasing with injected power (and thus what is transferred to the SOL) and that the ion source, I_{NET}, is *power-limited*. Also shown in Figure 26(b) is the maximum outer divertor ion source calculated assuming that **all** the power flowing into the outer divertor ionization region [$P_{NET} \sim 0.5 \bullet P_{SOL}$ - P_{Rad} (outer divertor)] is used for creation of ions from neutrals [30]. No power would be left to flow to the divertor plate. *The inferred ion source appears limited by the power flowing into the ionization region*. The further implication is that recombination is not the only reason for current loss at the plates; *it is not a necessary condition for detachment.* This inference is further supported by results with H-mode discharges. The levels of recombination in such discharges are negligible even though there is a significant plate

ion current loss during detachment [19,30]. It is also true that recombination does not play a significant role in the momentum loss associated with detachment.

The various scaling studies that were carried out for the ion sources and sinks also led to conclusions about the scaling of the density in the recombining region [30]. It was found that $n_{e,recomb} \sim \alpha x \bar{n}_e^{\beta} x P_{SOL}^{\gamma}$. The constants α, β, & γ were slightly different for the inner and outer divertor with β being the strongest scaling (.75 – 0.85). The discussion showed that such a scaling would be consistent with the recombining region being located in a region of local plasma pressure ~ 1/3 that of the upstream pressure, also consistent with previous modelling.

X. Measurements of radiation absorption

Since most of the 'complete' three-body recombinations occur by emission of Ly_α (~90%) or Ly_β (10%), any reduction in these channels due to photon re-absorption reduces the net recombination rate and increases the net ionization rate, thus affecting the overall divertor solution. After emission, resonance photons can be absorbed by neutral atoms in their paths, the amount of absorption increasing with increasing $N_0 \Delta L$, where N_0 is the neutral atom density along the path length ΔL. These absorbing, excited atoms can re-radiate or suffer ionizing collisions (as well as other collisions). If the atoms re-radiate, a photon can continue to diffuse through the absorbers (diffusion really being a process of absorption and reemission). However, if the excited atom is ionized before it de-excites, which we will term 'trapped', a Lyman photon has been lost and no net recombination has occurred, since the 'complete' recombination of the original atom has resulted in an ionization of an absorbing atom. Trapping and radiation transfer is a very complex problem in which diffusion both in space and wavelength occurs. The primary effect on the ionization/recombination balance is to lower the temperature at which they are

equal (for fixed n_e and N_0).

Photon trapping of hydrogenic Lyman series line emission will be very strong in the divertor of a Burning Plasma Experiment (BPX). For example, even though ITER is predicted to have neutral (N_0) and electron densities slightly lower than that of C-Mod, the divertor size (ΔL) would be ~ 10x larger. Likewise, for the largest existing divertor in JET, the path length is only a factor of 2 smaller than ITER but the neutral density is much lower. The recombination rate per unit volume (~ n_e^3) is much lower than in C-Mod. Because JET and C-Mod are closest to a BPX in terms of $N_0 \Delta L$, those experiments have allowed the only measurements of significant photon trapping effect to date [50,46]. The radiation transport of Lyman series emission in a MARFE at the midplane has been modeled in 1D [51]. Other, more simplified 1D treatments of tokamak-divertor–plasma conditions have been done [52,53]. Two-dimensional extensions of divertor radiation transport modelling is the subject of ongoing work [54]. Because the mean free path for photon absorption (~ 1 mm) is smaller than the divertor fan in C-Mod such data will be a good test of the models for ITER. The role of Ly_α trapping on C-Mod divertor neutral pressures has been studied as part of an effort to explain the high neutral densities in C-Mod [36,55]. Those initial results show that it is very important to include Ly_α trapping.

The trapping of $Ly_{\alpha,\beta}$ has been investigated experimentally on C-Mod by measuring the brightnesses of Ly_β and D_α with VUV and visible instruments whose midplane measurement chords were co-aligned in a view of the inner divertor just below the x-point. If Ly_β is optically thin, the brightnesses of these lines will be in the ratio of their spontaneous emission coefficients, i.e.,

$$B_{Ly_\beta} = B_{D_\alpha} \frac{A_{3\to1}}{A_{3\to2}} \tag{7}$$

However, if Ly_β is trapped, its brightness will decrease relative to that of D_α. Examples of no

trapping and trapping cases are shown in Figure 28a and b respectively. Ly_γ, and D_α are shown in Fig 28c for the same discharge as 28b indicating that Ly_γ is not trapped while there is significant trapping for Ly_β.

The systematic trend of increased trapping of Ly_β with increasing D_α emission (higher n_0, n_e) is shown in Fig. 29. At the highest D_α brightnesses, the transmission of Ly_β, $T_{Ly\beta}$, defined as of the ratio of the left-hand side to the right-hand side of Eq. 7, has decreased to ~50%. This transmitted fraction has been used to make a simple estimate of the atomic density in the emitting region based on the mean free path for absorption compared to the divertor size. This estimate was verified using a CR model. The CR model also allowed the effect of Ly_α and Ly_β trapping to be taken into account when determining the recombinations/photon in a recombining plasma. The effect is shown in Fig. 24.

XI. Summary

Alcator C-Mod research has yielded significant contributions to the understanding of divertor physics. This has been enabled by the many detailed diagnostic measurements, particularly Langmuir probes, spectroscopy, and bolometer tomography. The study of the effect of divertor geometry on detachment showed that utilization of a vertical divertor plate geometry led to lower detachment threshold than for more open, flat-plate, divertors. Other tokamaks, as well as the ITER design, have now switched to this geometry.

Early C-Mod measurements of detachment characteristics showed that very low electron temperatures (~ 1 eV) occur during detachment and the ion flux to the plate can drop by a factor of 10 or more. This was shown to be the result of pressure loss along the magnetic field. The

detachment studies that followed delved deeply into the how detachment develops (e.g. the movement of the detachment front towards the x-point) and the specifics of the requirements for detachment (collisionality, loss of power to the divertor…).

Spectroscopic techniques developed at C-Mod allowed the determination of the temperature, density and recombination rate within the detached region, giving the only quantitative measurement of the rate ions are converted to neutrals, thus confirming many of the 2D fluid models predictions of the role of recombination. A second spectroscopic technique developed at C-Mod allowed the determination of the Lyman beta radiation trapping rate from which one can estimate the trapping rate for Ly_{α}, which has been shown to affect the ionization balance in the divertor. More general investigations of the detached and recycling regimes confirmed that it was possible to dissipate the high parallel heat flux regimes available in C-Mod. The magnetic field direction can also strongly affect the balance of heat flow to the inner and outer divertors.

The characteristics of the C-Mod are similar or the same as those predicted for ITER in a number of aspects. Such characteristics include the high-Z Mo tiles, the vertical plate divertor, high parallel heat fluxes, neutral densities, and electron densities in the divertor. Together, they make studies of C-Mod divertor physics very relevant to understanding what will happen in a BPX like ITER in a number of areas. A few of those physics tests are the capability to develop detachment at high parallel power fluxes, whether predicted recombination rates match the code results, the effect of Lyman series absorption on the divertor characteristics (e.g. detachment), and high neutral density effects.

Acknowledgements

The authors thank the Alcator C-Mod operations group for expertly providing the discharges used in these studies. We would also like to thank several past members of the C-Mod team who made contributions – Garry McCracken, John Goetz, Chris Kurz, and Spencer Pitcher. This work is supported at MIT by DoE Contract No. DE-FC02-99ER5412.

Figure captions

Figure 1: Poloidal cross-section of the C-Mod vessel showing the closed, vertical-plate divertor at the bottom of the vessel and open divertor at the top. All tiles are made of molybdenum.

Figure 2: Divertor diagnostics: a) divertor probes and location of one of the divertor pressure gauges in the plenum behind the outer divertor. The 'nose' of the outer divertor is at the point closest to the x-point, probe 8. The 'nose' of the inner divertor is similarly located at inner divertor probe 4; b) divertor bolometer array.

Figure 3: Upstream (SOL) and downstream (divertor) profiles of electron pressure and T_e for three different divertor/SOL regimes – a) low-density or sheath-limited; b) high-recycling; and c) detached (from [24]).

Figure 4: Electron stagnation pressure, electron temperature, and density profiles at the scanning probe location and on inner and outer divertor surfaces for forward and reversed B_T directions are shown for a set of 800 kA, lower single-null, Ohmic plasmas ([16]).

Figure 5: Divertor measurements on the ρ=4.5 mm flux surface: a) Outside/inside electron temperature ratio, b) density ratio, and c/d) 'grounded' current density normalized to the ion saturation current density. All are plotted vs λ_{ei}/L (from [16]).

Figure 6: Private flux zone (PFZ) recombination rate as a function of peak electron pressure at the outer divertor leg when that region is attached (from [17]).

Figure 7: Parallel heat fluxes measured near the outer divertor strike point in an ICRF-heated L-mode discharge.

Figure 8: Radiation emissivity patterns (MW/m^{-3}) as reconstructed from divertor bolometer system showing attached, 'high-recycling', and 'detached divertor' cases (from [22]).

Figure 9: The ratio of radiation power occurring outside the separatrix (divertor) to inside the separatrix vs the input power. There is a shift in balance of radiation from outside to inside the separatrix when the divertor detaches (from [22]).

Figure 10: High power L-mode discharge with detachment induced by methane (CH_4) puffing (from [22]). Periods of detachment ('DD') and high-recycling ('HR') are labeled at the top of the figure.

Figure 11: The power reaching the divertor plates vs input power. Detached divertor regimes generally lead to lower power fluxes onto the divertor plates (from [22]).

Figure 12: Evolution of the outer divertor ion saturation currents as the plasma density is increased in an Ohmically-heated discharge. Ion saturation current traces are shown from probes located on the outer divertor (see Figure 2a). Detachment occurs at 0.73 seconds (from [21]).

Figure 13: Electron temperature (a) and density (b) at outer divertor probe location 7 as line-averaged density normalized to plasma current is increased (from [24]). The approximate correspondence to the Greenwald density fraction is also shown.

Figure 14: Ratio of total plasma pressures upstream to that at the divertor plate as a function of divertor plate electron temperature. Data are shown from a large number of discharges and for 4 locations outside the separatrix (ρ is the distance from the separatrix referenced to the midplane).

Figure 15: Tomographic reconstruction of D_γ emissivities, showing the evolution of detached plasma regions with increased density (from [17]).

Figure 16: Comparison of divertor bolometer signals with and without neutral gas 'filter' for charge-exchange neutrals (from [29]). Detachment starts at 0.6s for this L-mode shot. The ICRF causes the plasma to reattach over most of the divertor plate.

Figure 17: Effect of neon injection on the density threshold for divertor detachment (from [35]). The change in Z_{eff} due to the increased Ne is also shown. The Greenwald fraction at a line averaged density of $2x10^{20}$ m^{-3} is $n_e/n_{Greenwald} \sim 0.35$.

Figure 18: Effect of increased SOL power on initially detached divertor (from [35]). The electron pressure (a), density (b) and temperature (c) at the outer divertor plate are shown for 3 flux surfaces outside the separatrix given by ρ. In the last panel (d) the divertor radiation, derived from tomography, that is emitted from regions inside ($P_{rad,div,in}$) and outside ($P_{rad,div,out}$) the

separatrix are give along with the power flowing into the SOL, P_{SOL}. The line shown is for $P_{rad,div,out} = P_{SOL}$.

Figure 19: Typical core plasma conditions are shown for an attached EDA H-mode plasma without nitrogen puffing (dashed lines) and a dissipative divertor H-mode plasma with nitrogen puffing (solid lines) [19]. The H-mode transition (for both plasmas) occurs at 0.61 (vertical dash-dotted line), the gas puff begins at 0.7, and the outer divertor begins to detach at 0.83 s (vertical dotted line) when the plasma pressure (and heat flux) at the outer divertor strike point drops by more than a factor of 10. The injected ICRF power is shown with the dotted line in (a) and is nearly the same for both plasmas. [Dashed lines: Shot 980213007; solid lines: Shot 980213015.] The divertor radiated power increases from 1 to 1.6 MW after the nitrogen injection. [19]

Figure 20: Three divertor geometries, used to investigate the effect of divertor plate inclination on the detachment threshold (from [37]): a) standard 'vertical plate' divertor, b) 'slot' divertor and c) 'flat-plate' divertor.

Figure 21: Flux surface extent of divertor detachment as a function of density. For vertical- and slot divertor geometries the detached region extends to the outer divertor 'nose' (see Figure 2a) location (from [37]). Detachment occurs at $\bar{n}_e \sim 1.4 \times 10^{20}$ m^{-3} ($n_e/n_{Greenwald} \sim 0.24$) for the 'slot-geometry', at $\bar{n}_e \sim 1.8 \times 10^{20}$ m^{-3} ($n_e/n_{Greenwald} \sim 0.31$) for the 'vertical-plate', and at $\bar{n}_e \sim 2.8 \times 10^{20}$ m^{-3} ($n_e/n_{Greenwald} \sim 0.47$) for the 'flat-plate'.

Figure 22: Outer divertor (square & circle symbols) and upstream (+ symbols) electron temperatures at the $\rho = 2$ mm flux surface for flat-plate and vertical-plate geometries versus line-

averaged density (from [37]). Detached cases are indicated with filled symbols. See Figure 21 caption for range of $n_e/n_{Greenwald}$.

Figure 23: (a) Detachment threshold density versus $L_{X,connect}$ and (b) corresponding strike-point locations on outer divertor for five geometries studied (from [37]).

Figure 24: Recombinations per D_γ photon as a function of local electron temperature (from [46]) for cases in which the emission region is optically-thin (diamond symbols) and thick (square symbols) to hydrogen Lyman series radiation.

Figure 25: Typical D^0 recombining spectra in the VUV (a) and visible (b). Dashed line in (a) represents a radiative recombination model with emission region length = 1.5 cm, $n_e=1.8x10^{21}$ m^{-3}, $T_e=0.7$ eV. (c) A Voigt fit to the 8→2 Balmer line to obtain Stark width and n_e. (d) Fit of Saha distribution to D^0 population densities to obtain T_e (from [30]).

Figure 26: (a) Ion sinks for the outer divertor plate in 1MA Ohmic detachment (starts at ~0.75 sec.) where $\bar{n}_e$ is increased continuously until 1.0 seconds; $I_{Sink}=I_{Plate}+I_{Recomb}$. (b) Comparison of the inferred outer divertor ion source to $\bar{n}_e^2$ (scaled to match I_{Sink} at 0.4 seconds) and the net power flowing into the outer divertor ionization region converted to ion flux [$I_{NET}=P_{NET}/(e\bullet 30\text{ eV})$]. (from [30]).

Figure 27: Divertor recombination and plate ion sinks for two different plasma currents vs. $\bar{n}_e$. 0.8MA: I_R (●), I_P (——). 1MA: I_R (❑), I_P (- - - -). Also shown is the total recombination, including that inside the separatrix, for both currents (— —). (from [30]).

Figure 28: Ly_β (solid line) and scaled D_α (symbols) brightnesses for untrapped Ly_β (a) and trapped Ly_β and (b) cases. (c) The time history of Ly_γ (dashed line) for the same discharge as (b), indicating that Ly_γ and D_α stay in a constant ratio, unlike Ly_β and D_α. (from [46]).

Figure 29: (a) The scaling of the transmitted fraction of Ly_β versus the D_α brightness. (b) The scaling of the ratio of Ly_α to D_α brightnesses (measured in photons/s/cm2/sr) versus the D_α brightness (from [46]).

References

[1]B. LABOMBARD and B. LIPSCHULTZ, Nuclear Fusion 27, 81 (1987).

[2]B. LIPSCHULTZ, B. LABOMBARD, E.S. MARMAR et al., Nuclear Fusion 24, 977 (1984).

[3]B. LIPSCHULTZ, B. LABOMBARD, H.L. MANNING et al., Nuclear Fusion 26, 1463 (1986).

[4]B. LIPSCHULTZ, B. LABOMBARD, E. S. MARMAR et al., Journal of Nuclear Materials 128-129, 555 (1984).

[5]E. MARMAR, M. FOORD, B. LABOMBARD et al., Journal of Nuclear Materials 121, 69 (1984).

[6]J.E. RICE, E.S. MARMAR, B. LIPSCHULTZ et al., Nuclear Fusion 24, 329 (1984).

[7]D.B. MONTGOMERY, J.H. SCHULTZ, R.J. THOME et al., Proceedings of the 10th Symposium on Fusion Engineering Proceedings (Cat. No. 83CH1916-6 NPS), 5-9 Dec. 1983, Philadelphia, PA, USA, 1983 (IEEE), Vol. 2, pp. 2101-2105.

[8]B. LIPSCHULTZ, D.B. MONTGOMERY, P.A. POLITZER et al., Journal of Nuclear Materials 121, 441 (1984).

[9]D. B. MONTGOMERY, H. BECKER, M. BESEN et al., Proceedings of the 12th Symposium on Fusion Engineering, Monterey, CA, 1987 (Vol. 1, pp. 11-14.

[10]D. POST, W. HOULBERG, G. BATEMAN et al., Physica Scripta T16, 89 (1987).

[11]D.M. MEADE, Journal of Fusion Energy 7, 229 (1988).

[12]A. LOARTE, R.D. MONK, J.R. MARTIN-SOLIS et al., Nuclear Fusion 38, 331 (1998).

[13]G. FEDERICI, C.H. SKINNER, J.N. BROOKS et al., Nuclear Fusion 41, 1967 (2001).

[14]I. H. HUTCHINSON, B. LABOMBARD, J. A. GOETZ et al., Plasma Physics & Controlled Fusion 37, 1389 (1995).

[15]I. H. HUTCHINSON, J. A. GOETZ, D. F. JABLONSKI et al., Plasma Physics and Controlled Fusion 38, 24 (1996).

[16]B. LABOMBARD, J. A. GOETZ, I. HUTCHINSON et al., Journal of Nuclear Materials 241-243, 149 (1997).

[17]C.J. BOSWELL, J.L. TERRY, B. LABOMBARD et al., Journal of Nuclear Materials 290-293, 556 (2001).

[18]F.W. PERKINS, D.E. POST, N.A. UCKAN et al., Nuclear Fusion 39, 2137 (1999).

[19]J. A. GOETZ, B. LABOMBARD, B. LIPSCHULTZ et al., Physics of Plasmas 6, 1899 (1999).

[20]ITER PHYSICS EXPERT GROUP ON DIVERTOR, ITER PHYSICS EXPERT GROUP ON DIVERTOR MODELLING AND DATABASE, and ITER PHYSICS BASIS EDITORS, Nuclear Fusion 39, 2391 (1999).

[21]B. LIPSCHULTZ, J. GOETZ, B. LABOMBARD et al., Journal of Nuclear Materials 220-222, 50 (1995).

[22]J. A. GOETZ, C. KURZ, B. LABOMBARD et al., Physics of Plasmas 3, 1908 (1996).

[23]G. M. MCCRACKEN, R. S. GRANETZ, B. LIPSCHULTZ et al., Journal of Nuclear Materials 241-243, 777 (1997).

[24]B. LABOMBARD, J. GOETZ, C. KURZ et al., Physics of Plasmas 2, 2242 (1995).

[25]O. V. BATISHCHEV, A. A. BATISHCHEVA, P. J. CATTO et al., Journal of Nuclear Materials 241-243, 374 (1997).

[26]P.C. STANGEBY, Nuclear Fusion 33, 1695 (1993).

[27]C. KURZ, B. LA BOMBARD, B. LIPSCHULTZ et al., Plasma Physics & Controlled Fusion 39, 963 (1997).

[28]C. S. PITCHER, J. A. GOETZ, B. LABOMBARD et al., Journal of Nuclear Materials 266-269, 1009 (1999).

[29]B. LIPSCHULTZ, J. L. TERRY, C. BOSWELL et al., Physical Review Letters 81, 1007 (1998).

[30]B. LIPSCHULTZ, J. L. TERRY, C. BOSWELL et al., Physics of Plasmas 6, 1907 (1999).

[31]M. GREENWALD, J. L. TERRY, S. M. WOLFE et al., Nuclear Fusion 28, 2199 (1988).

[32]G. F. MATTHEWS, Journal of Nuclear Materials 220-222, 104 (1995).

[33]P. C. STANGEBY, Physics of Fluids 28, 644 (1985).

[34]P. C. STANGEBY, *The plasma boundary of magnetic fusion devices* (Institute of Physics Pub., Bristol, UK ; Philadelphia, PA, 2000).

[35]B. LIPSCHULTZ, J. A. GOETZ, B. LABOMBARD et al., Elsevier. Journal of Nuclear Materials 241-243, 771 (1997).

[36]B. LIPSCHULTZ, B LABOMBARD, S. LISGO et al., "Neutrals studies in Alcator C-Mod," *submitted to Fusion Science & Technology*,

[37]B. LIPSCHULTZ, J. GOETZ, I. HUTCHINSON et al., Proceedings of the 14th Int. Conf. on Plasma Physics and Controlled Fusion Research, Montreal, 1996 (IAEA, Vienna).

[38]K. BORRASS, D. COSTER, D. REITER et al., Journal of Nuclear Materials 241-243, 250 (1997).

[39]S. I. KRASHENINNIKOV, AYU PIGAROV, D. A. KNOLL et al., Physics of Plasmas 4, 1638 (1997).

[40]A. LOARTE, Journal of Nuclear Materials 241-243, 118 (1997).

[41]D. LUMMA, J. L. TERRY, and B. LIPSCHULTZ, Physics of Plasmas 4, 2555 (1997).

[42]R.C. ISLER, G.R. MCKEE, N.H. BROOKS et al., Physics of Plasmas 4, 2989 (1997).

[43]G.M. MCCRACKEN, M.F. STAMP, R.D. MONK et al., Nuclear Fusion 38, 619 (1998).

[44]U. WENZEL, K. BEHRINGER, A. CARLSON et al., Nuclear Fusion 39, 873 (1999).

[45]R.C. ISLER, R.W. WOOD, C.C. KLEPPER et al., Physics of Plasmas 4, 355 (1997).

[46]J. L. TERRY, B. LIPSCHULTZ, AYU PIGAROV et al., Physics of Plasmas 5, 1759 (1998).

[47]L. C. JOHNSON and E. HINNOV, Journal of Quantitative Spectroscopy & Radiative Transfer 13, 333 (1973).

[48]R. D. BENGSTON and J. D. TANNICH, Physics Letters A 1, 532 (1970).

[49]C. S. PITCHER and P. C. STANGEBY, Plasma Physics & Controlled Fusion 39, 779 (1997).

[50]T. LOVEGROVE, L. D. HORTON, R. W. T. KONIG et al., Proceedings of the 22nd EPS Conference on Plasma Physics & Controlled Fusion, Bournemouth, UK, 1995 (Vol. 19C - Part III, pp. 301.

[51]M.L. ADAMS, H.A. SCOTT, R.W. LEE et al., Journal of Quantitative Spectroscopy and Radiative Transfer 71, 117 (2001).

[52]S.I. KRASHENINNIKOV and A.YU. PIGAROV, Contributions to Plasma Physics 28, 443 (1988).

[53]A.S. WAN, H.E. DALHED, H.A. SCOTT et al., Journal of Nuclear Materials 220-222, 1102 (1995).

[54]D. REITER, S. WIESEN, and M. BORN, Journal of Nuclear Materials 313-316, 845 (2003).

[55]S. LISGO, P. BORNER, C. BOSWELL et al., Journal of Nuclear Materials 337-339, 139 (2005).

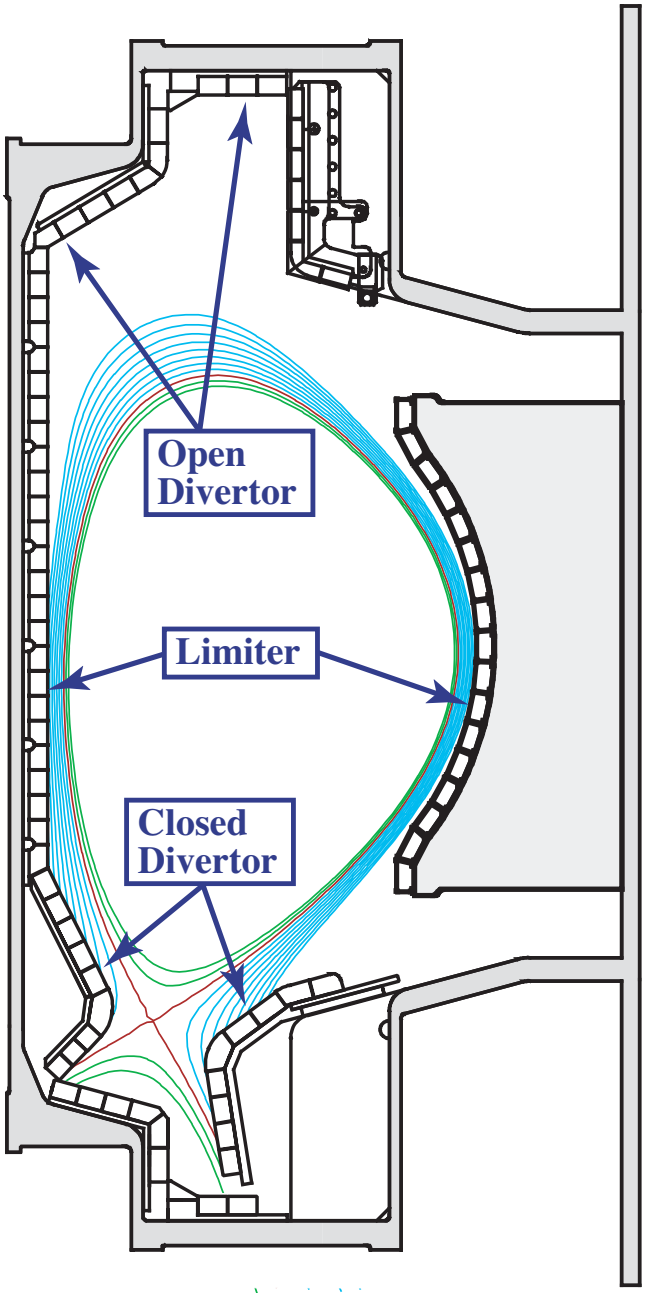

Figure 1: Divertor physics research on
Alcator C-Mod, Lipschultz et al.

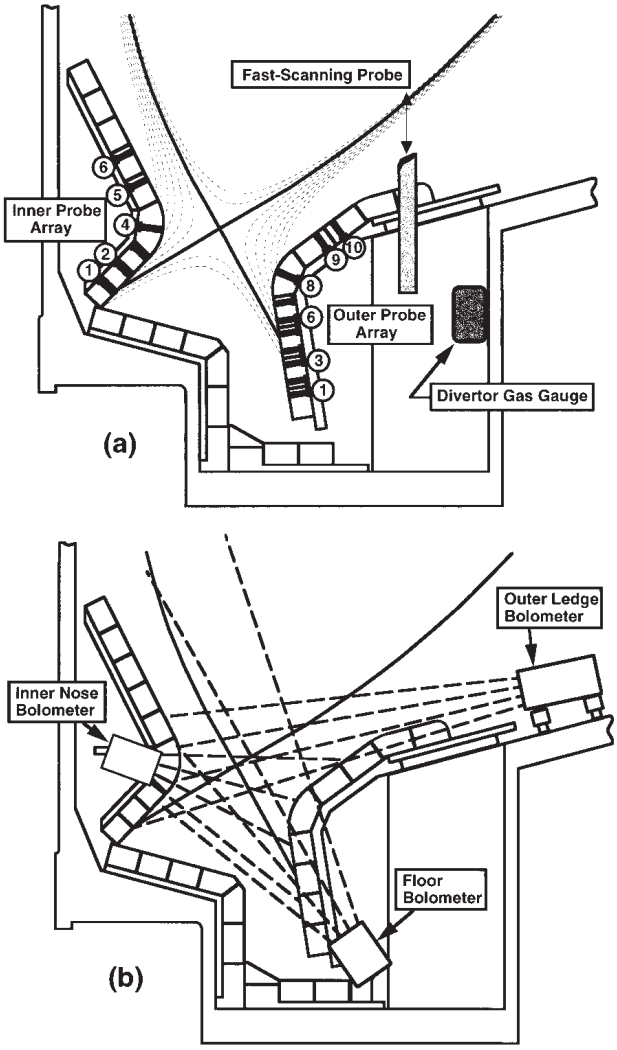

Figure 2: Divertor physics research on Alcator C-Mod, Lipschultz et al.

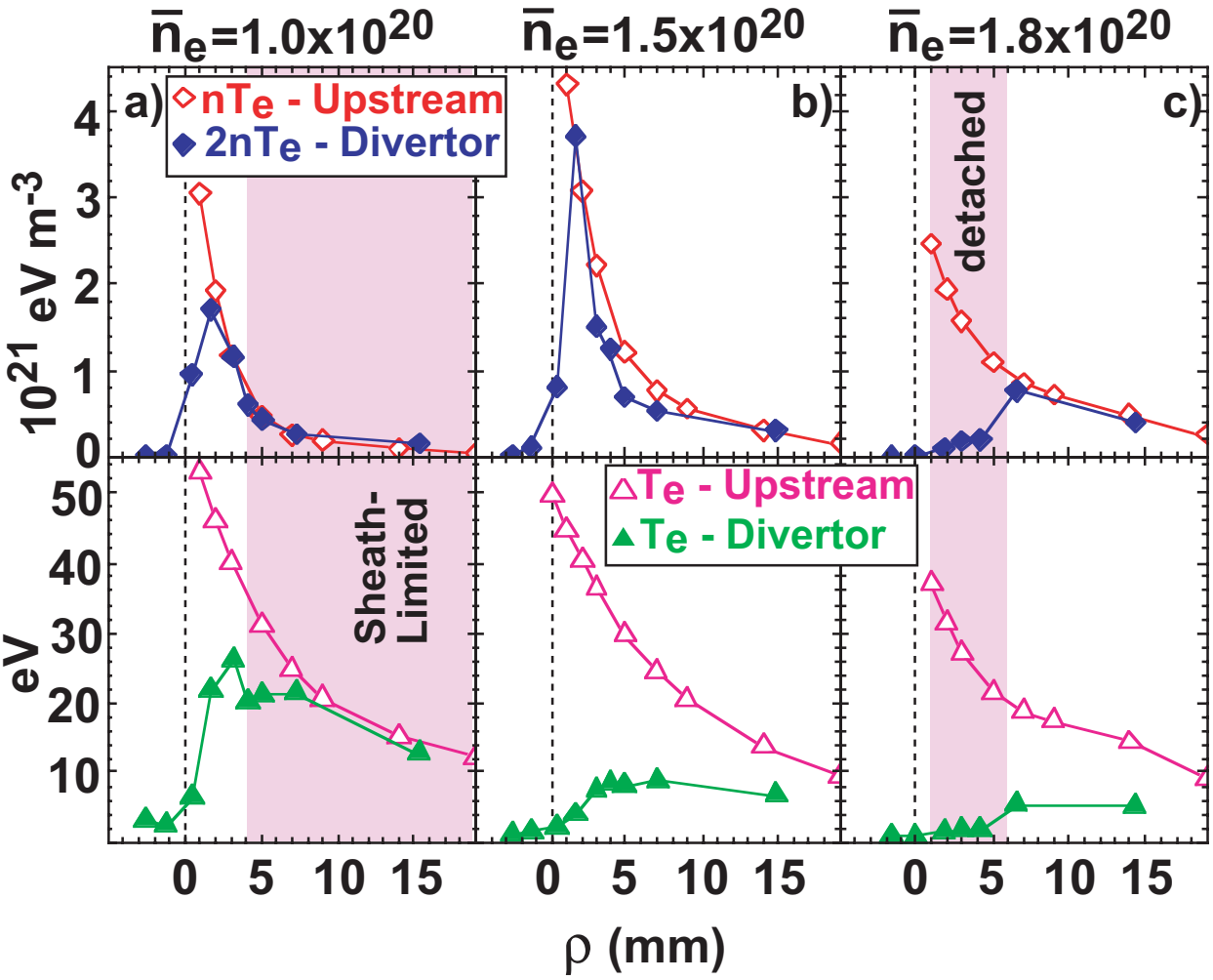

Figure 3: Divertor physics research on Alcator C-Mod, Lipschultz et al.

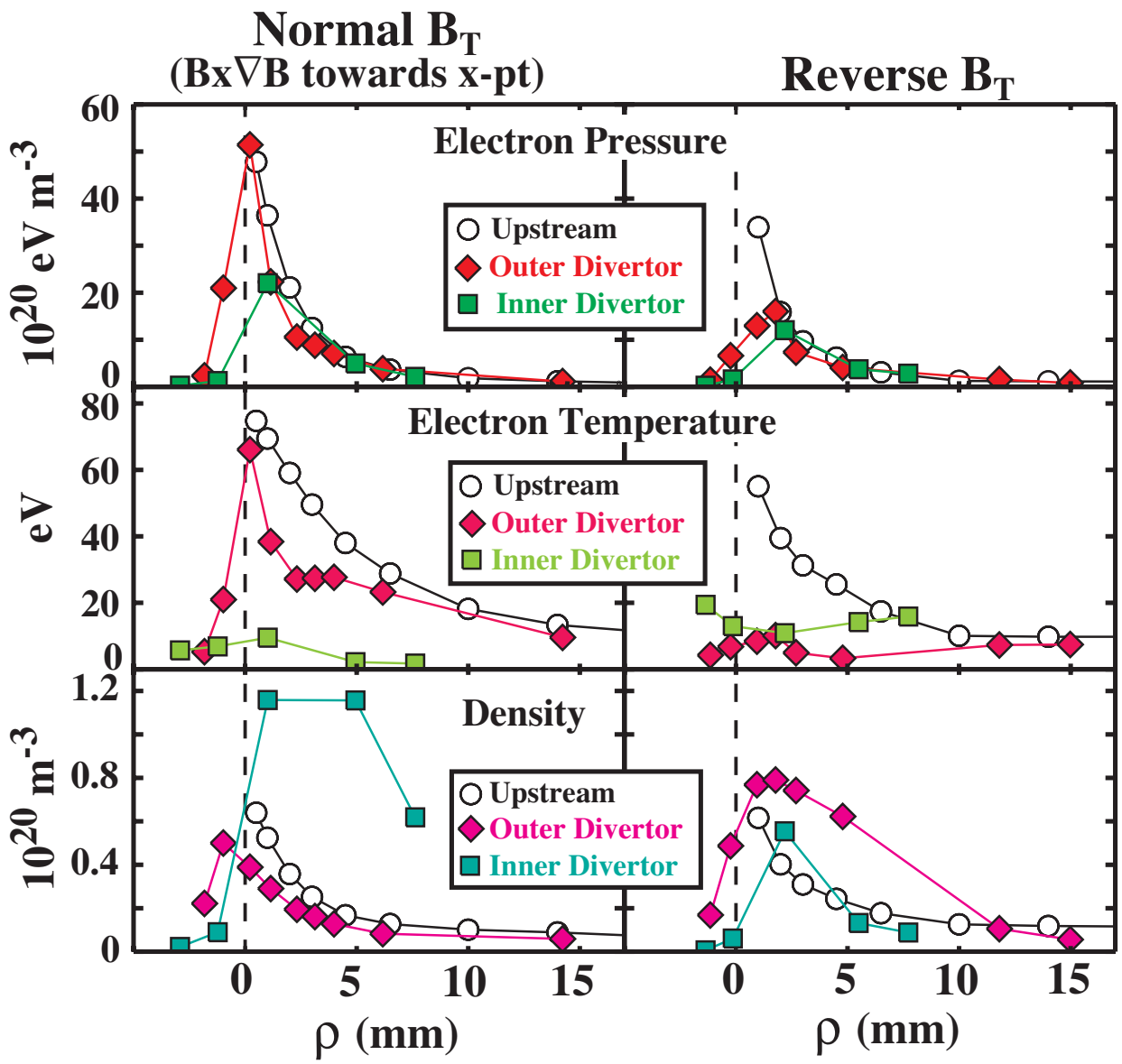

Figure 4: Divertor physics research on Alcator C-Mod, Lipschultz et al.

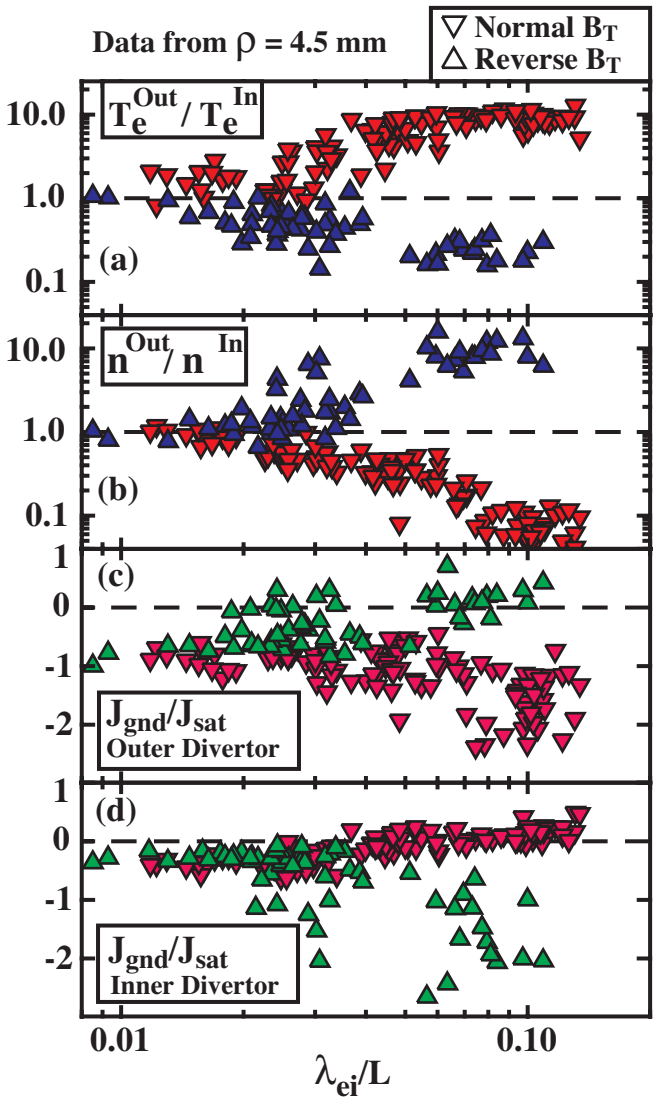

Figure 5: Divertor physics research on Alcator C-Mod, Lipschultz et al..

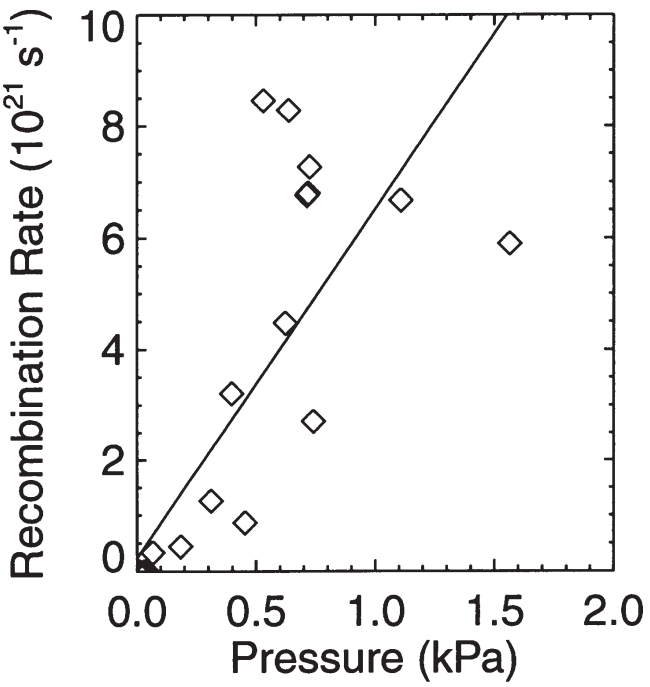

Figure 6: Divertor physics research on Alcator C-Mod, Lipschultz et al.

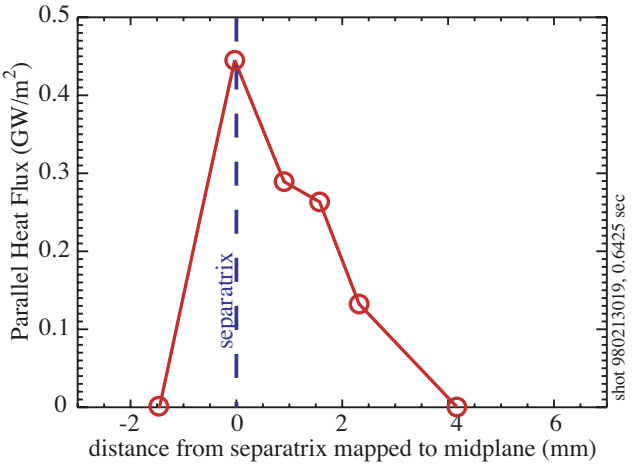

Figure 7: Divertor physics research on Alcator C-Mod, Lipschultz et al.

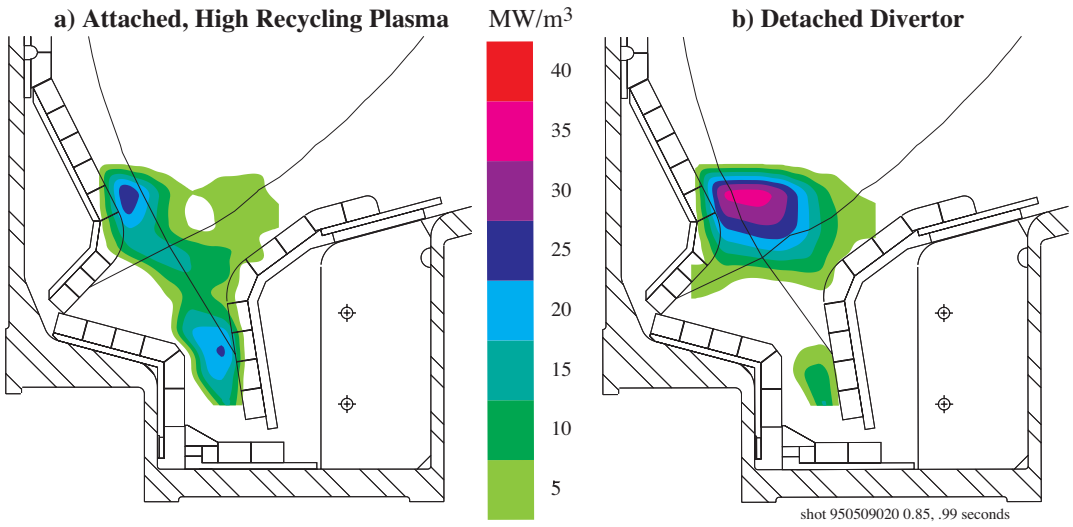

Figure 8: Divertor physics research on Alcator C-Mod, Lipschultz et al.

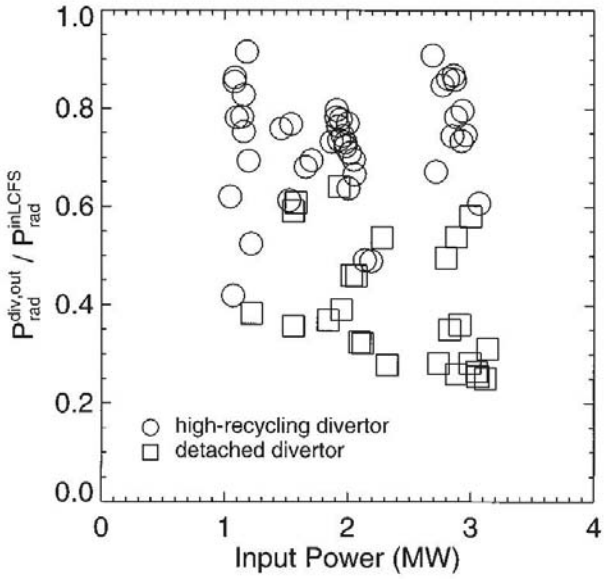

Figure 9: Divertor physics research on Alcator C-Mod, Lipschultz et al.

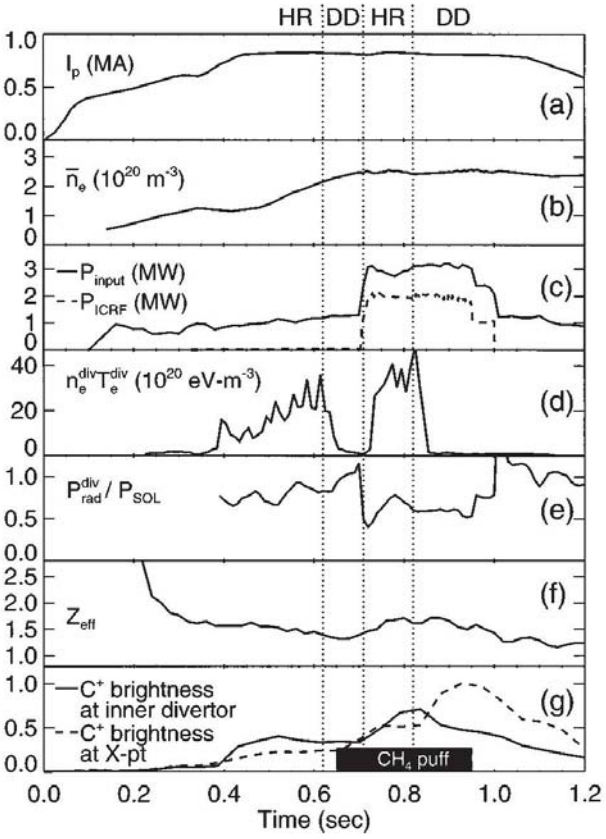

Figure 10: Divertor physics research on Alcator C-Mod, Lipschultz et al.

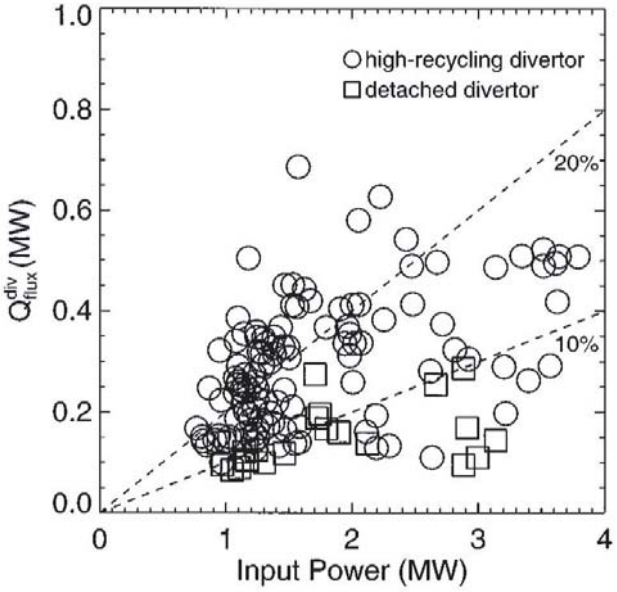

Figure 11: Divertor physics research on Alcator C-Mod, Lipschultz et al.

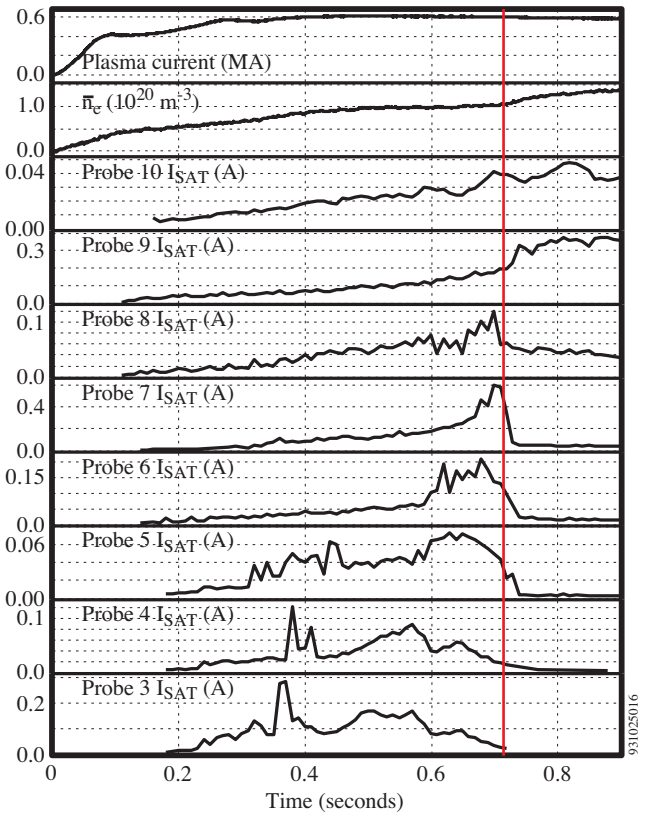

Figure 12: Divertor physics research on Alcator C-Mod, Lipschultz et al.

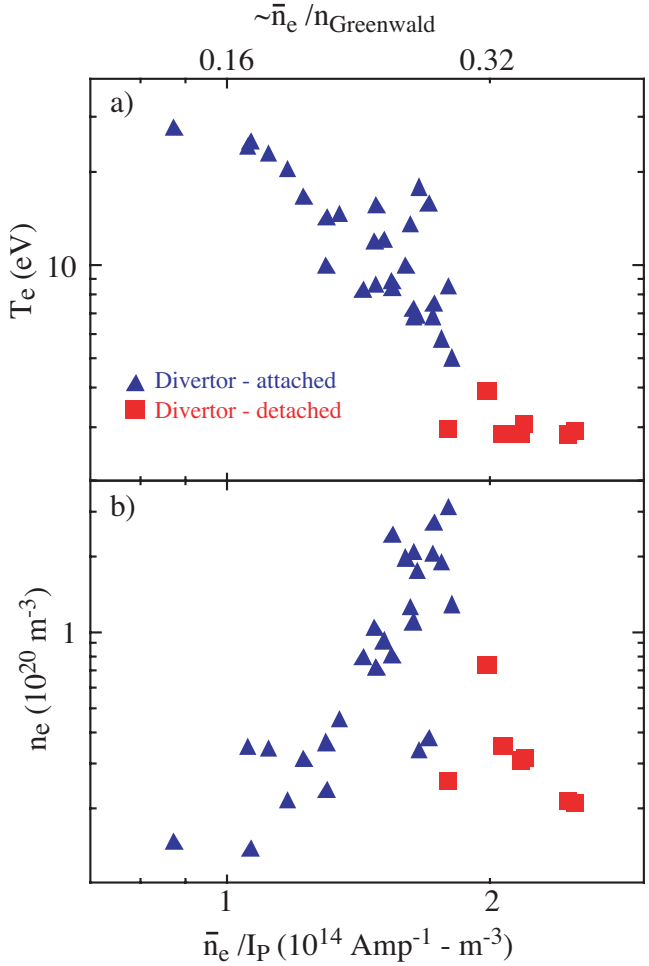

Figure 13: Divertor physics research on Alcator C-Mod, Lipschultz et al.

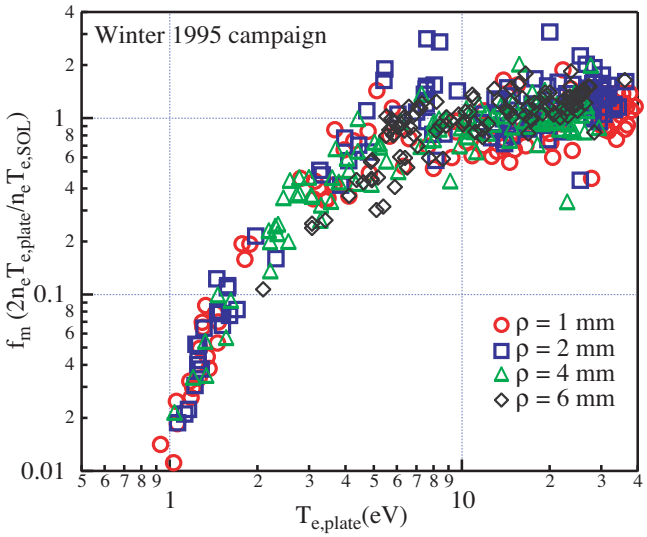

Figure 14: Divertor physics research on Alcator C-Mod, Lipschultz et al.

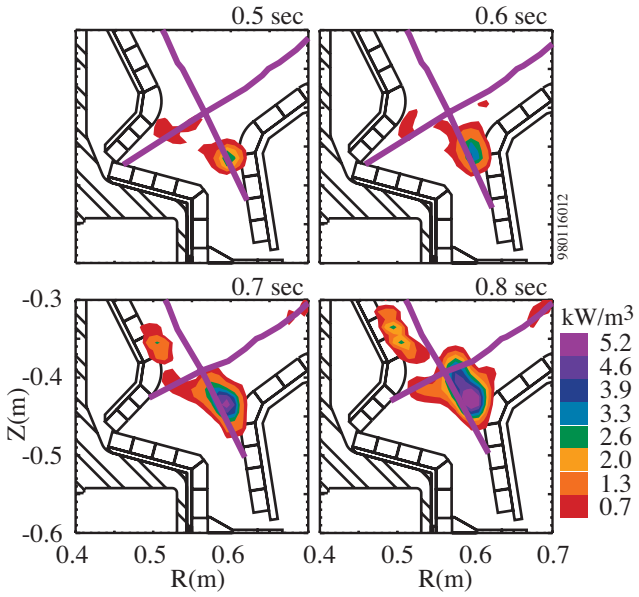

Figure 15: Divertor physics research on Alcator C-Mod, Lipschultz et al.

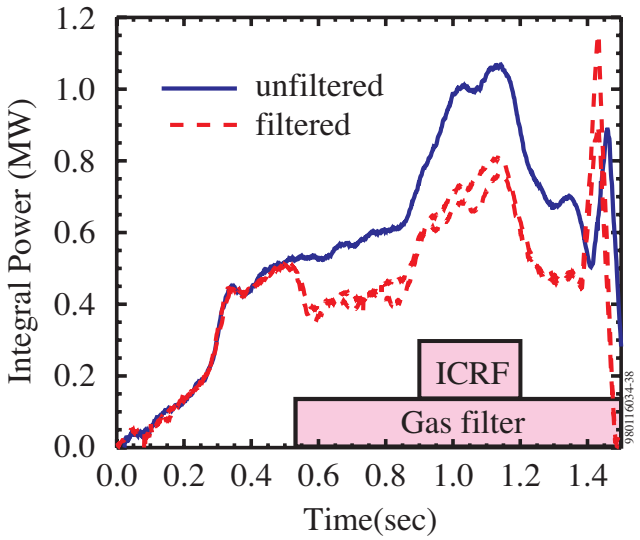

Figure 16: Divertor physics research on Alcator C-Mod, Lipschultz et al.

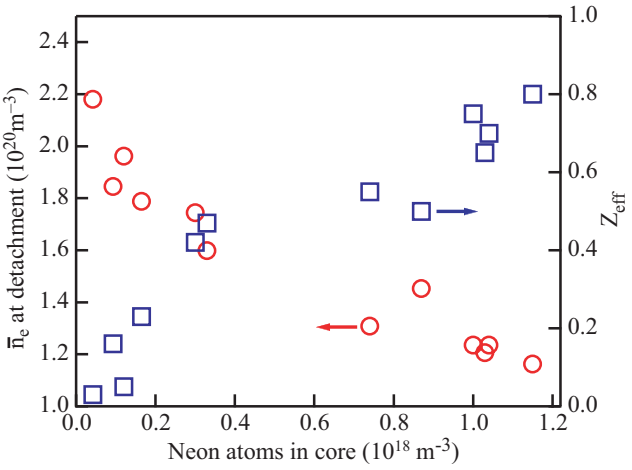

Figure 17: Divertor physics research on Alcator C-Mod, Lipschultz et al.

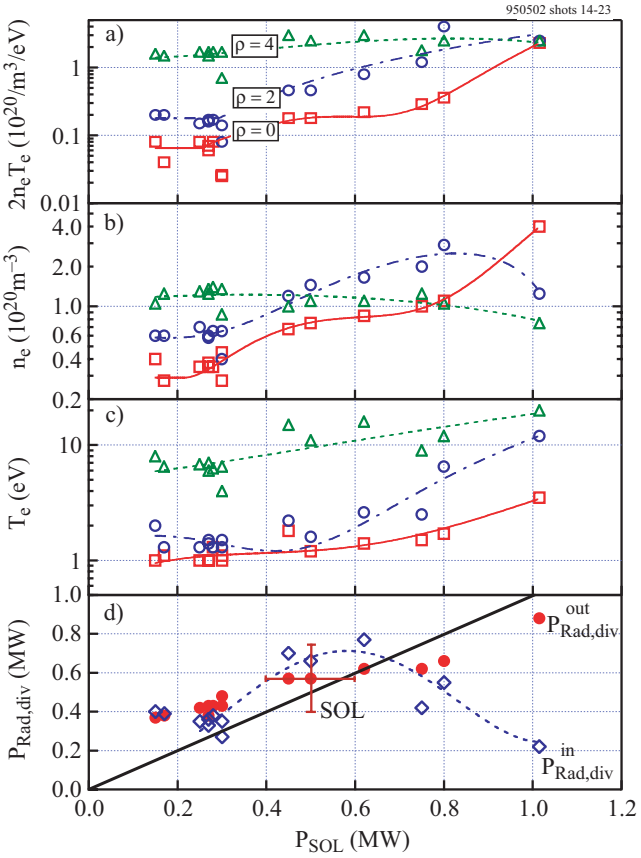

Figure 18: Divertor physics research on Alcator C-Mod, Lipschultz et al.

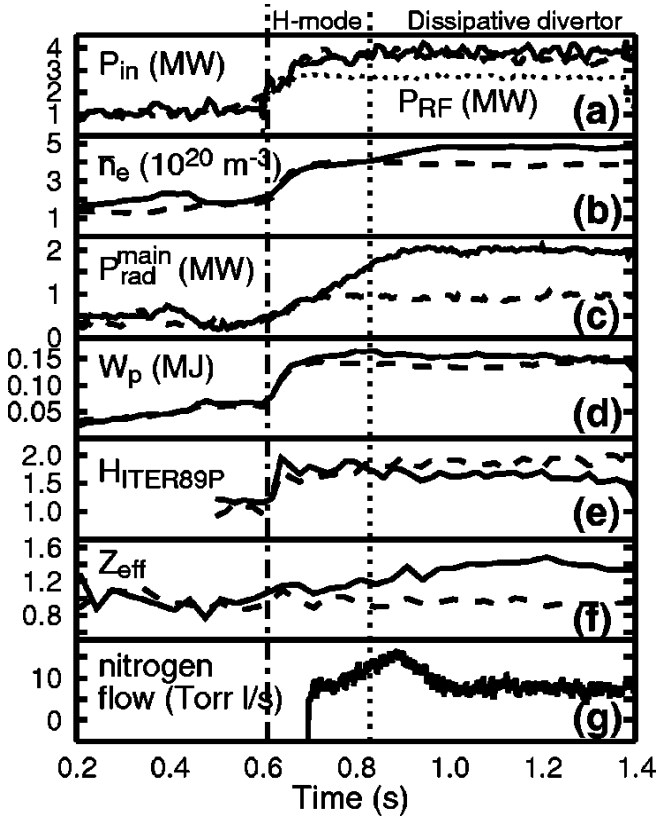

Figure 19: Divertor physics research on Alcator C-Mod, Lipschultz et al.

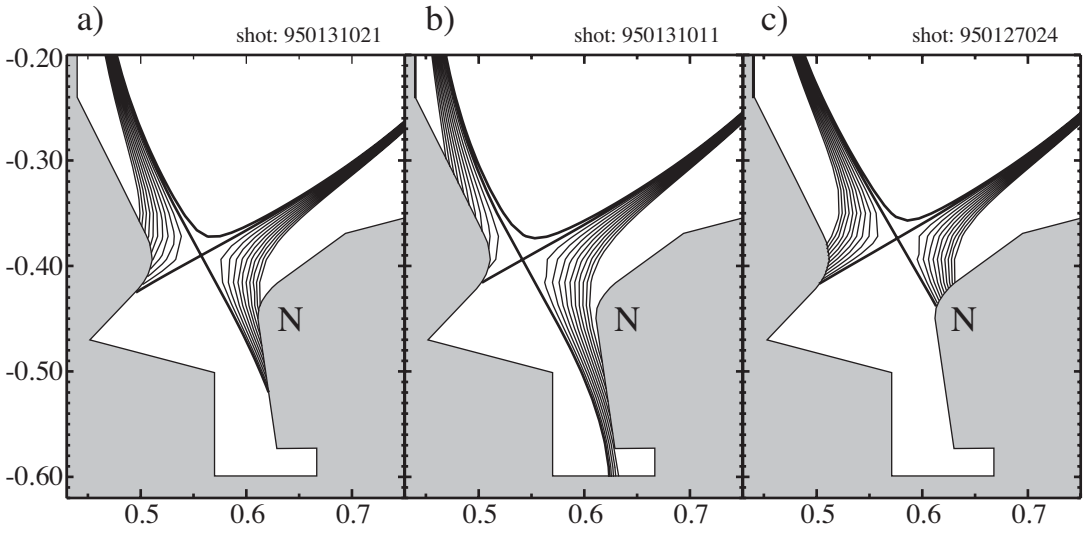

Figure 20: Divertor physics research on Alcator C-Mod, Lipschultz et al.

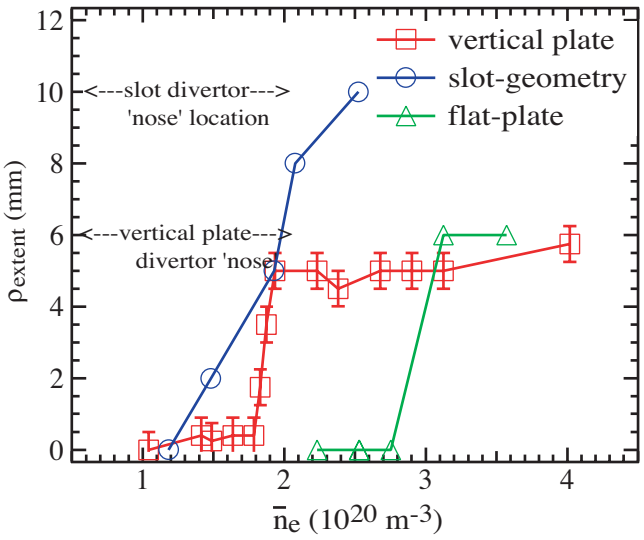

Figure 21: Divertor physics research on Alcator C-Mod, Lipschultz et al.

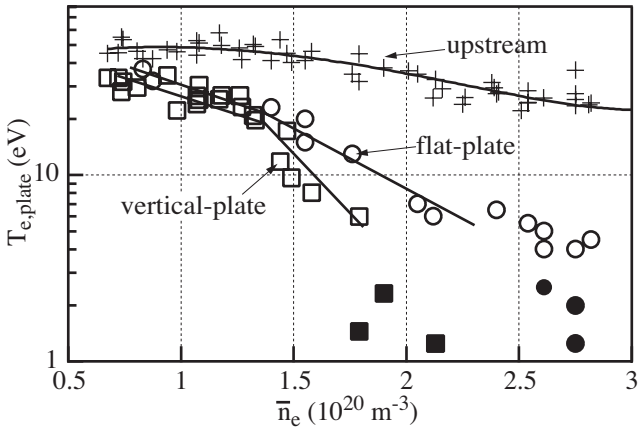

Figure 22: Divertor physics research on Alcator C-Mod, Lipschultz et al.

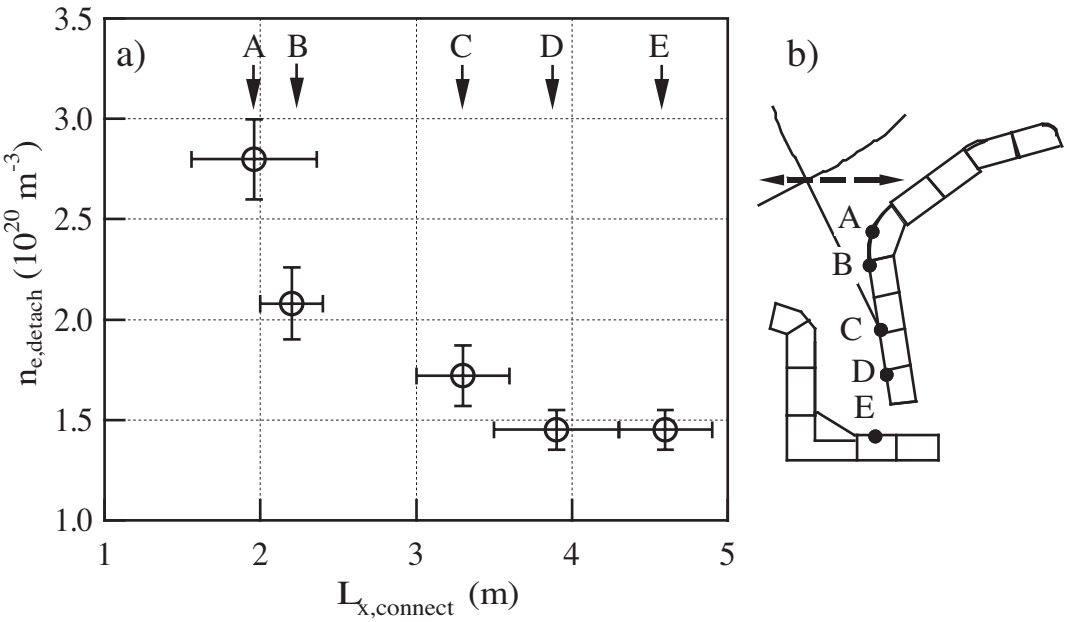

Figure 23: Divertor physics research on Alcator C-Mod, Lipschultz et al.

Figure 24: Divertor physics research on
Alcator C-Mod, Lipschultz et al.

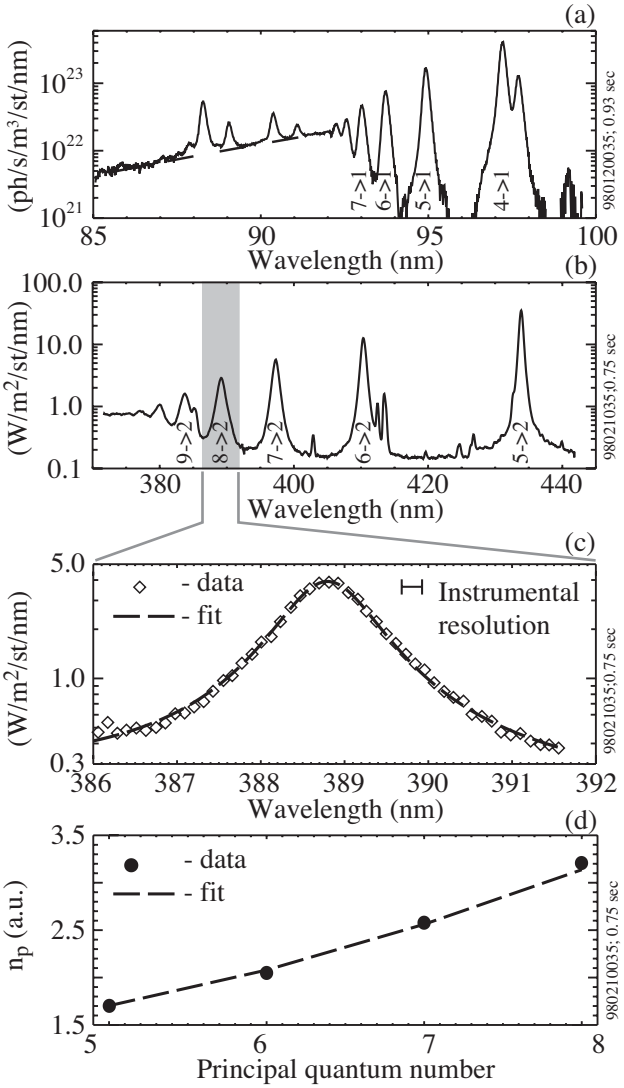

Figure 25: Divertor physics research on Alcator C-Mod, Lipschultz et al.

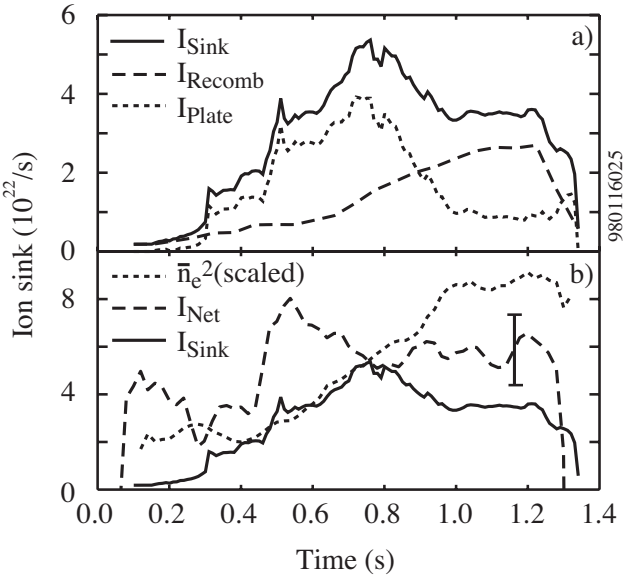

Figure 26: Divertor physics research on Alcator C-Mod, Lipschultz et al.

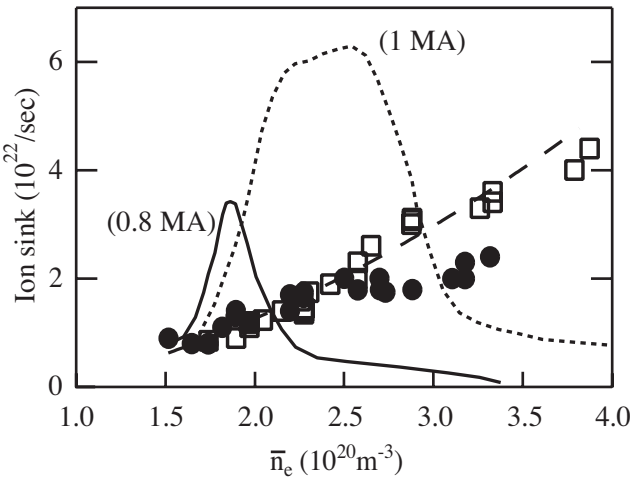

Figure 27: Divertor physics research on Alcator C-Mod, Lipschultz et al.

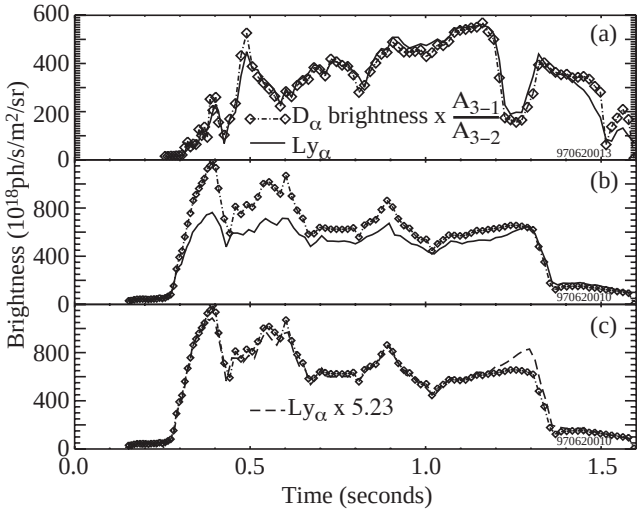

Figure 28: Divertor physics research on Alcator C-Mod, Lipschultz et al.

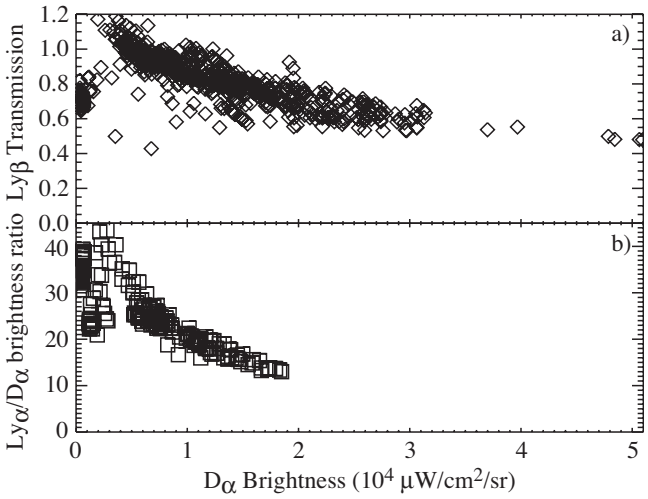

Figure 29: Divertor physics research on Alcator C-Mod, Lipschultz et al.